NASA CR-183,021

COMPUTATIONAL DESIGN OF LOW ASPECT RATIO WING-WINGLET CONFIGURATIONS FOR TRANSONIC WIND-TUNNEL TESTS

by

John M. Kuhlman and Christopher K. Brown

Progress Report
for the Period Jan. 1 - June 30, 1988

Grant NAG-1-625
NASA Langley Research Center
Hampton, VA 23665
Mr. Richard L. Campbell, Technical Monitor
Transonic Aerodynamics Division

COMPUTATIONAL DESIGN OF LOW ASPECT RATIO WING-WINGLET CONFIGURATIONS FOR TRANSONIC WIND-TUNNEL TESTS

by

John M. Kuhlman and Christopher K. Brown

SUMMARY

A computational design has been performed for three different low aspect ratio wing planforms fitted with nonplanar winglets; one of the three planforms has been selected to be constructed as a wind tunnel model for testing in the NASA LaRC 7 x 10 high speed wind tunnel. A design point of M = 0.8, $C_L \cong 0.3$ was selected, for wings of aspect ratio equal to 2.2, and leading edge sweep angles of 45° and 50°. Winglet length is 15% of the wing semispan, with a cant angle of 15°, and a leading edge sweep of 50°. Winglet total area equals 2.25% of the wing reference area. This report summarizes the design process and the predicted transonic performance for each configuration.

INTRODUCTION

Winglets have proven to be effective nonplanar drag reduction devices in several applications to high aspect ratio wing planforms typical of transport or business jet aircraft. However, recent studies have indicated even larger potential benefits may be obtained when winglets are used on low aspect ratio configurations such as fighter aircraft (Refs. 1-3). It was found in the computational work of Refs. 1-3 that one can obtain the same percentage reduction in drag coefficient at the same C_L and ratio of winglet length-to-wing span, independent of wing aspect ratio and leading edge sweep, even at the transonic design point selected for the current work. Since a low aspect ratio wing has a lower lift-to-drag ratio than a high aspect ratio wing, then an equal percentage reduction in drag coefficient at equal lift

coefficient results in a larger drag force reduction at low-aspect ratio.

DESIGN PROCEDURE

The present work has been undertaken to design a low aspect ratio wing-winglet wind tunnel model to be constructed and tested in the NASA LaRC 7 x 10 high speed tunnel, to confirm the numerical drag reduction predictions of Refs. 1-3. Designs have been performed for three different wing planforms, all using the same design procedure developed in Refs. 1-2. For each wing planform, an optimum wing-alone geometry and a wing-winglet geometry have been defined. A linear potential flow theory design code (Refs. 4, 5) has been used to define wing-winglet and wing-alone camber surfaces for minimum induced drag at the selected design point of M = 0.8, $C_L \cong 0.3$. This design point was chosen as being representative of a cruise condition for heavily loaded lightweight fighters at an altitude of 30,000 feet. The design code was run at $C_L = 0.4$, because addition of a fuselage was found to reduce the calculated C_L by approximately 0.1. A NACA 64A006 thickness distribution has been added to the camber surface, and a cylindrical fuselage having a diameter equal to 0.125b, and 5.25b in length has been used. For all wing-winglet configurations the wing and winglet geometry have been altered in the vicinity of the wing-winglet juncture, to reduce loading and eliminate or reduce the strength of any shocks formed in this region. Wing tip airfoil camber has been reduced, and geometric incidence has been reduced for the outboard 10% of the wing, while winglet toe out has been increased at the winglet root, following the procedures which were developed in Refs. 1-3. Also, for all current designs an a = 0.8 chordwise loading shape function has been utilized in an effort to elliminate any predicted upper surface trailing edge boundary layer separation, such as was found for the earlier designs which used an a = 1.0 rectangular loading (Ref. 1). This procedure was

successful at eliminating predicted upper surface boundary layer separation for an aspect ratio 2.20 wing-winglet and wing in Ref. 3. Figs. 1 and 2, taken from Ref. 3, summarize these results. Typical pressure coefficient distributions for the A = 2.20, Λ = 45° wing-winglet are shown in Fig. 1 for designs using a = 1.0, 0.9, and 0.8 chordwise loading functions at M = 0.8, α = 0°. Pressure recovery on the upper surface is more gradual as the value of a is reduced, but shocks on the winglet are strengthened slightly. As stated in Ref. 3, there was no predicted boundary layer separation on the wing for the a = 0.8 configuration. As shown in Fig. 2, all three chordwise loading functions yielded essentially the same calculated drag polars. The wing-winglet geometry for this planform is shown in Fig. 3.

Performance predictions for the wing-alone and wing-winglet configurations versus angle of attack have been obtained using the WIBCO-PPW transonic small disturbance code of Refs. 6,7, at M = 0.8. Calculated force coefficients, spanloads, and boundary layer separation locations on the wing will be presented for all three wing planforms and the three corresponding wing-winglet configurations. Also, typical calculated pressure coefficient distributions will be presented.

PLANFORM DESCRIPTIONS

Two planforms previously studied in Ref. 1 have been used in the present design effort. These wing planforms were called cases F and G in Ref. 1. Also, a third planform has been studied which is essentially configuration G with an unswept trailing edge (called cropped delta G in this study). Definition of these three wing planforms is given in Table 1, while Figs. 3-5 show the resulting wing-winglet design geometries without the fuselage for cases F, G, and cropped delta G, respectively. Wing F has a leading edge sweep of 45° and A = 2.2, while wing G has Λ = 50°, A = 2.2. Both of these

wings have a taper ratio of 0.2. The cropped delta G has an unswept trailing edge, with $\Lambda = 50°$, A = 2.22, and $\lambda = .203$.

All 3 wing-winglet configurations have winglet planforms with $\Lambda = 50°$ and a taper ratio of 0.5. Winglet root chord is 60% of the wing tip chord and winglets have been mounted in an aft position. Winglet cant has been fixed at 15° from the vertical, and all winglets have used a NACA 64A006 thickness distribution. These winglet planform choices are similar to those used in refs. 1-3, and are similar to design recommendations by Whitcomb (Ref. 8) for winglets mounted on transport type wings. Winglet total area is 2.25% of the wing reference area for configurations F and G, and 2.27% for configuration cropped delta G.

Wing-alone design geometries obtained from the linear design code have not been altered. However, in order to obtain successfully converged transonic flow predictions for the wing-winglet geometries using the WIBCO-PPW code, it was necessary to modify the linear theory camber surfaces in the wing-winglet juncture region, as discussed in Refs. 1,2, to reduce loading in this region. In addition, for the a = 0.8 chord loading used in the present study it was necessary to further reduce loading in the wing-winglet juncture as shown in Table 2.

PRESENTATION OF PERFORMANCE RESULTS

Predicted performance results to be presented include lift and drag coefficients, pitching moment and wing root bending moment coefficients, typical pressure coefficients, normalized spanloads, and upper surface wing boundary layer separation locations for the wing-alone and the wing-winglet configurations for all three wing planforms, generally for $-4° \leq \alpha \leq 0°$. Note that all force and moment coefficients presented include only the forces and moments on the wing and winglet, but omit those on the fuselage. Viscous

effects on the winglet are estimated using an empirical skin friction correlation. All results for configurations G and cropped delta G have been obtained using 150 crude grid iterations, followed by 150 crude-fine grid iterations using the interacted Bradshaw strip boundary layer on the wing, at a Reynolds number of 3.8 x 10^6 based upon wing mean aerodynamic chord. This is estimated to be a realistic Reynolds number for the wind tunnel model. Results for configuration F (partly taken from Ref. 3) have been obtained using 100 crude grid iterations, followed by 200 crude-fine grid iterations with the interacted strip wing boundary layer at a Reynolds number of 9 x 10^6. Boundary layer transition has been assumed to occur at x/c = 0.05.

Note that for both the wing-alone and wing-winglet configuration F, no converged solutions could be obtained for $\alpha > 0.5°$, while all G and cropped delta G configurations would not converge for $\alpha > 0°$. The same difficulty was encountered in Refs. 1-3 for the previous geometries using an a = 1.0 rectangular chord loading. However, for the present configurations using a = 0.8 chord loadings this difficulty in obtaining converged solutions while including the viscous boundary layer calculation at higher lift coefficients seems to be worsened. Note also that results for a modified cropped delta G wing-winglet are presented (Table 2), where further unloading of the wing-winglet juncture by increased winglet root toe out and wing tip twist was successful at increasing the angle of attack for which converged solutions could be obtained up to $\alpha = 1°$ ($C_L = 0.3344$, versus $C_L = 0.2934$ at $\alpha = 0°$).

The calculated performance prediction results are presented in the following figures: (Force coefficients are also presented in Table 3)

Results	Figure Numbers
Configuration F Force Coefficients	6
Configuration F Spanloads	7

DISCUSSION OF RESULTS

Force Coefficients

Predicted lift and moment coefficients for each of the three different basic wing planforms all look quite similar, and all vary linearly versus angle of attack. Generally, wing-winglet configurations develop slightly less lift at the same α than the corresponding optimum wing-alone configuration. This is due to the modifications which were required in the wing-winglet juncture to reduce loading in this region. Note, however that the effect of adding a winglet to a fixed wing geometry may be seen in Fig. 21 by comparing the wing-winglet C_L with that of the wing of the wing-winglet design (diamond symbols). Addition of a winglet not only reduces C_D somewhat due to the thrust on the winglet but also increases C_L by about 5% (by .016 at $C_L \cong .293$ and by .011 at $C_L \cong .206$).

Drag polars and L/D versus C_L also all look similar, where the drag polars appear to be shifted downwards to lower drag levels for the wing-winglet configurations relative to the corresponding optimum wing-alone

configurations. Predicted percentage reductions in C_D at equal C_L are presented in Table 4 for all three wing planforms for C_L between 0.18 and 0.26. Note that predicted percent reduction in C_D tends to decrease slightly as C_L increases, and that these percent reductions are comparable for all three wing planforms.

Pitching moment coefficients about the wing apex are not altered greatly for wing-winglet configurations. For example, for the cropped delta G, C_m is increased 1.5% at C_L = .18 and 1.9% at C_L = .26 for the wing-winglet relative to the wing-alone. Wing root bending moment coefficients for wing-winglet configurations are increased by about 5-6% relative to the corresponding wing-alone case at equal lift. For the cropped delta G, increases are 5.4% at C_L = .18 and 6.0% at C_L = .26. These percentage increases are consistent with those observed in Refs. 1-3, and are expected to be related to the wing structural weight penalty due to the winglet.

Spanloads

Predicted spanload distributions have been normalized by C_L, so total area under the curve should equal one and be independent of angle of attack. Spanload results are shown typically at α = 0°, -2°, -4°, for both the wing-alone and the wing-winglet configurations. Spanload shape does not change greatly with angle of attack for the wing-alone configurations. However, there is a noticeable, consistent trend for all wing-winglet spanloads for the normalized loading to be reduced as angle of attack is increased in the vicinity of the wing-winglet juncture, with a corresponding increase in inboard loading. Loading near the centerline is reduced for all configurations, due to the fuselage. This shifts the loading center outboard, and results in higher local Mach numbers on the wing upper surface near the wing tip than otherwise would be required to develop a given C_L value. Loading is higher

than elliptical near the wing tip of the wing-alone configurations. Also, loading outboard on the wing is higher than the theoretical optimum for wing-winglet configurations, except at the wing tip. Loading is also reduced relative to the linear theory theoretical optimum at the winglet root. Similar trends were observed in Refs. 2,3.

Boundary Layer Separation

Comparison of predicted wing boundary layer separation locations shows a great deal of difference between the three wing planforms. None of the configurations have any predicted boundary layer separation on the wing lower surface for $-4° \leq \alpha \leq 0°$. The configuration F wing-alone and wing-winglet results show essentially no predicted upper surface boundary layer separation, as first reported in Ref. 3. However, both the G and cropped delta G configurations have predicted boundary layer separation on the wing upper surface, which tends to worsen as α is reduced.

This is shown most clearly in Fig. 39 where predicted upper surface separation locations at M = 0.8, $\alpha = 0°$ are compared for the three wing-alone designs and the four wing-winglet designs. Note that results for the modified cropped delta G wing-winglet are for $\alpha = -0.5°$, because the solution at $\alpha = 0°$ experienced difficulties in the boundary layer calculation. Neither the F or G wing-alone configurations have any predicted boundary layer separation, while the cropped delta G wing has predicted separation near the trailing edge for $0.23 < \eta < .34$ and $.66 < \eta < .9$. No boundary layer separation is observed for the configuration F wing-winglet, while both configurations G and cropped delta G have predicted boundary layer separation over the entire wing, from the wing-body juncture, where separation is predicted at $x/c \cong .985$ to the vicinity of the wing-winglet juncture where separation is predicted at $x/c \cong .93$. The modified cropped delta G is somewhat better, but still has predicted

upper surface boundary layer separation outboard of η = .76.

This trend of increasingly worse trailing edge boundary layer separation as the wing trailing edge sweep is increased (from -12° for configuration F, to -1.2° for G, to 0° for the cropped delta G) is consistent with trends observed for shock-induced trailing edge separation on a series of arrow wings at M > 1 in Refs. 9,10. However, there is no evidence of any trailing edge shock for any of the present results. Hence, the predicted boundary layer separation locations from the WIBCO-PPW code have been monitored versus the iteration count, as summarized in Table 5. Generally, the predicted separation region initially grows and then decreases in size as the iteration count increases. The predicted separation region may be further reduced in size or even be eliminated with a greater number of iterations. Also, it is expected that the reduced number of initial crude grid iterations used for configuration F (100 versus 150) may have influenced the boundary layer separation prediction, by reducing the steepness of any regions of rapid pressure recovery.

In an effort to obtain an independent measure of the reliability of the boundary layer separation prediction for the G and cropped delta G configurations, the shock-induced trailing edge separation criterion developed by Cunningham, et al., (Ref. 11) has been used to analyze the airfoil geometry of these configurations, as shown in Table 6. Here the incidence angle for onset of shock-induced trailing edge separation, α_{ted}, is tabulated, calculated according to the method developed in Ref. 11. Airfoil geometric parameters used in this method include the nondimensional radius of curvature at the airfoil upper surface crest, c/R, and the lower surface and camber line slopes at the airfoil trailing edge, δ_{tel} and δ_{tec}, respectively. Here, if the value of α_{ted} is negative, then shock-induced trailing edge separation is predicted to have already occurred, while $\alpha_{ted} > 0$ indicates that separation should not

occur until $\alpha > \alpha_{ted}$. Comparison of Table 6 and Fig. 39 shows that the separation prediction using Ref. 11 shows the same trend as the strip boundary layer calculation in WIBCO-PPW.

Pressure Coefficient Distributions

Pressure coefficient distributions for all configurations appear quite similar to one another at nearly equal C_L values. Also, C_p distributions on the wing of each wing-winglet configuration are essentially identical to those of the corresponding wing-alone configuration except at the wing tip, where the presence of the winglet results in additional loading. Pressure distributions at $\alpha = 0°$ all are quite similar to those obtained previously in Refs. 1-3. Use of the a = 0.8 chordwise loading function results in more gradual pressure recovery on the upper surface near the trailing edge relative to results with a = 1.0, as seen previously in Ref. 3. Mid-chord shocks are found on the inboard surfaces of the lower half of the winglets for all four wing-winglet configurations for $\alpha > -2°$ ($C_L > 0.2$). Calculated pressure distributions change quite significantly versus angle of attack, even though there is not much variation in normalized spanload.

As angle of attack is decreased to $\alpha = -4°$, pressure suction spikes are observed on the lower surfaces of all wing-alone and wing-winglet configurations near the leading edge. The level of these suction spikes at $\alpha = -4°$ appear to be quite similar for all 3 wing-alone and 4 wing-winglet configurations. The development of such leading edge suction spikes is due to the relatively small nose radius of the 64A006 thickness distribution utilized for the present design geometries.

Pressure distributions for the two wings analyzed for the cropped delta G planform are quite similar. However the wing of the wing-winglet design has slightly greater suction on the upper surface near the leading edge.

Calculated upper and lower surface pressure distributions on the winglet, and on the wing near the tip, are at times observed to cross near the trailing edge. This is believed to be due to the frozen streamwise wake modeling utilized in the WIBCO-PPW code.

CONCLUSION

Predicted transonic flow performance results have been presented for seven different low aspect ratio configurations (three wing designs and four wing-winglet designs) for a design point of $M = 0.8$, $C_L \cong 0.3$. All wing-winglet designs yield the same predicted percent drag reduction relative to the corresponding wing-alone design. However, since it is felt that the cropped delta G wing planform is most representative of wing planforms for current and next generation fighter wings, this will be the configuration which will be constructed for the wind tunnel test, even though this planform had the worst predicted boundary layer separation characteristics. The modified cropped delta G wing-winglet and cropped delta G wing-alone geometries will be constructed to fit to a simplified cylindrical fuselage with an ogive nose, to allow a fair comparison between the drag of the wing-winglet relative to the wing-alone. Predicted drag reductions due to the winglet of about 12% at $C_L = 0.26$, neglecting the fuselage, should correspond to about a 6-8% total drag reduction when the fuselage forces are included.

Since the configurations selected for the wind tunnel test do have some predicted boundary layer separation, it is recommended that some redesign of both configurations be performed using the automated design method of Smith (Ref. 12), which uses the methodology of the airfoil design method of Campbell (Ref. 13). In particular, pressure recovery should be made more gradual near the trailing edge, to eliminate the predicted trailing edge boundary layer separation for both the wing-alone and wing-winglet designs. Also, it may be

possible to improve flow in the vicinity of the wing-body juncture. It may also be desirable to increase the nose radius slightly to reduce the leading edge pressure spikes away from the design point. However, this may be a disadvantage when the model is tested at supersonic Mach numbers.

Note that the uncambered airfoils having significant positive geometric incidence which are found at the wing root for all of the present designs (Figs. 3-5) are similar to those obtained for higher aspect ratio wings using automated optimization methods and transonic analysis codes, as found in Refs. 14,15. In Reference 14 the starting airfoil geometries included aft-cambered supercritical sections at the wing root, but the twisted, uncambered final root airfoils reduced the configuration drag.

Future efforts will be aimed at obtained WIBCO-PPW performance predictions for the cropped delta G configurations using the actual fuselage geometry, once the fuselage geometry has been finalized. Results will be obtained both with the viscous boundary layer calculation, as well as without the boundary layer to obtain results at higher C_L values. Also, performance predictions will be obtained using the cylindrical TAG grid version of PPW developed by Rosen (Ref. 16), and the store carriage code of Ref. 17. This code utilizes rotated finite differences to better capture shocks at higher C_L and can be run at low supersonic Mach numbers. Finally, construction of a low aspect ratio wing-winglet model designed at M = 0.1 will be completed, and the configuration will be tested in the WVU low speed wind tunnel at velocities of 100-200 ft/sec.

REFERENCES

1. Kuhlman, J. M. and Liaw, P., "Winglets on Low Aspect Ratio Wings," Paper AIAA-87-2482CP, presented at AIAA 5th Applied Aerodynamics Conference, Aug. 17-19, 1987, Monterey, CA; accepted for publication in J. of Aircraft.

2. Kuhlman, J. M., Liaw, P., and Cerney, M. J., "Theoretical/Numerical Study of Feasibility of Use of Winglets on Low Aspect Ratio Wings at Subsonic and Transonic Mach Numbers to Reduce Drag," NASA CR, 1988.

3. Kuhlman, J. M., Cerney, M. J., and Liaw, P., "Transonic Low Aspect Ratio Wing-Winglet Designs," Paper AIAA-87-0007, presented at AIAA 26th Aerospace Sciences Meeting, Jan. 11-14, 1988, Reno, NV.

4. Kuhlman, J. M. and Shu, J.-Y., "Computer Program Documentation for a Subcritical Wing Design Code Using Higher Order Farfield Drag Minimization," NASA CR-3457, September 1981.

5. Kuhlman, J. M., "Higher Order Farfield Drag Minimization for a Subcritical Wing Design Code," J. of Aircraft, Vol. 17, No. 9, September 1980, pp. 648-655.

6. Boppe, C. W. and Stern, M. A., "Simulated Transonic Flows for Aircraft with Nacelles, Pylons, and Winglets," Paper AIAA-80-0130, presented at AIAA 18th Aerospace Sciences Meeting, Pasadena, CA, January 14-16, 1980.

7. Boppe, C. W., "Aerodynamic Analysis of Aircraft with Nacelles, Pylons, and Winglets at Transonic Speeds," NASA CR-4066, April 1987.

8. Whitcomb, R. T., "A Design Approach and Selected Wind-Tunnel Results at High Subsonic Speeds for Wing-Tip Mounted Winglets," NASA TN D-8260, July 1976.

9. Kulfan, R. M. and Sigalla, A., "Real Flow Limitations in Supersonic Airplane Design," Paper AIAA-78-147, presented at AIAA 16th Aerospace Sciences Meeting, Jan. 16-18, 1978, Huntsville, Alabama.

10. Rettie, I., "Computer-Aided Aerodynamic Design for Supercruise," presented at Super Cruise Military Aircraft Design Conference, Feb. 17-20, 1976, Colorado Springs, CO.

11. Cunningham, A. M., Jr., Spragle, G. S., and Plentovich, E. B., "Constant-Shock-Jump C_p for Shock-Induced Trailing-Edge Separation," Paper AIAA-87-2553, presented at AIAA 5th Applied Aerodynamics Conference, Aug. 17-19, 1987, Monterey, CA; also NASA CR-4090, Aug. 1987.

12. Smith, L. A., "PPWFLEX: A Method for the Design of Transonic Flexible Wings," M.S. Thesis, School of Engineering and Applied Science, George Washington University, Feb. 1988.

13. Campbell, R. L. and Smith, L. A., "A Hybrid Algorithm for Transonic Airfoil and Wing Design," Paper AIAA-87-2552, presented at AIAA 5th Applied Aerodynamics Conference, Aug. 17-19, 1987, Monterey, CA.

14. Haney, H. P., Johnson, R. R., and Hicks, R. M., "Computational Optimization and Wind Tunnel Test of Transonic Wing Designs," Paper AIAA-79-0080, presented at AIAA 17th Aerospace Sciences Meeting, Jan. 15-17, 1979, New Orleans, LA; see Fig. 12.

15. Henne, P. A., "An Inverse Transonic Wing Design Method," Paper AIAA-80-0330, presented at AIAA 18th Aerospace Sciences Meeting, Jan. 14-16, 1980, Pasadena, CA; see Figs. 13,14.

16. Rosen, B. S., "Computational Transonic Analysis of Canted Winglets," J. of Aircraft, Vol. 21, No. 11, November 1984, pp. 873-878; also Paper AIAA-84-0302.

17. Rosen, B. S., "External Store Carriage Loads Prediction of Transonic Speeds," Paper AIAA-88-0003, presented at AIAA 26th Aerospace Sciences Meeting, Jan. 11-14, 1988, Reno, NV.

Table 1. Wing Planform Definition

1.	CASE F	A = 2.2	TR = 0.2	SWEEP = 45°
2.	CASE G	A = 2.2	TR = 0.2	SWEEP = 50°
3.	CROPPED DELTA G	A = 2.22	TR = 0.203	SWEEP = 50°

Table 2. Incidence Variation for Wing-Winglets at M = 0.8 Using a = 0.8 Chord Loading

	Change in Wing Tip Incidence at η = (0.91,0.97,1.0)	Change in Winglet Incidence at ζ = (0,.42,.80,1.0)
CASE F	0°, 0°, -1°	-5°, -3°, -1°, 0°
CASE G	-0.6°, -1.2°, -1.3°	-3.9°, -2.5°, -0.9°, 0°
CROPPED DELTA G	-0.6°, -1.2°, -1.3°	-3.9°, -2.5°, -0.9°, 0°
MODIFIED CROPPED DELTA G	-1°, -1.8°, -1.9°	-4.5°, -3°, -0.9°, 0°

Table 3. Calculated Force and Moment Coefficients

Configuration F

α	C_L	C_D	C_m	C_B	Configuration
0.0	.28616	.01870	-.2546	.14628	FWING
-1.0	.24538	.01380	-.2265	.12551	FWING
-2.0	.20326	.00984	-.1971	.10390	FWING
-3.0	.16040	.00700	-.1670	.08178	FWING
-4.0	.11432	.00568	-.1345	.05765	FWING
0.0	.27881	.01536	-.2522	.15118	FWWLT
-1.0	.23507	.01077	-.2205	.12803	FWWLT
-2.0	.19042	.00740	-.1882	.10422	FWWLT
-3.0	.14428	.00541	-.1548	.07949	FWWLT
-4.0	.09667	.00514	-.1206	.05371	FWWLT

Configuration G

α	C_L	C_D	C_m	C_B	Configuration
0.0	.29192	.01978	-.2908	.15008	GWING
-0.5	.27466	.01779	-.2786	.14144	GWING
-1.0	.25110	.01504	-.2580	.12936	GWING
-1.5	.22984	.01303	-.2408	.11838	GWING
-2.0	.21174	.01173	-.2280	.10910	GWING
-2.5	.18979	.01014	-.2099	.09760	GWING
-3.0	.16652	.00887	-.1905	.08545	GWING
-3.5	.14347	.00806	-.1717	.07355	GWING
-4.0	.12070	.00773	-.1535	.06153	GWING
0.0	.29390	.01770	-.2937	.15984	GWWLT
-0.5	.27124	.01516	-.2744	.14766	GWWLT
-1.0	.	.	.	.	GWWLT
-1.5	.22679	.01102	-.2373	.12376	GWWLT
-2.0	.20481	.00954	-.2194	.11196	GWWLT
-2.5	.18225	.00831	-.2008	.09979	GWWLT
-3.0	.15923	.00745	-.1818	.08705	GWWLT
-3.5	.13388	.00685	-.1601	.07361	GWWLT
-4.0	.11043	.00693	-.1412	.06060	GWWLT

Table 3. (Concluded) - Calculated Force and Moment Coefficients

Configuration Cropped Delta G

α	C_L	C_D	C_m	C_B	Configuration
0.0	.29279	.01971	-.2907	.15044	CWNGOPT
-0.5	.27364	.01746	-.2761	.14097	CWNGOPT
-1.0	.25238	.01511	-.2587	.12999	CWNGOPT
-1.5	.23003	.01295	-.2402	.11848	CWNGOPT
-2.0	.21162	.01165	-.2270	.10920	CWNGOPT
-2.5	.18708	.00981	-.2058	.09622	CWNGOPT
-3.0	.16658	.00890	-.1902	.08556	CWNGOPT
-3.5	.14299	.00808	-.1708	.07332	CWNGOPT
-4.0	.11959	.00777	-.1519	.06092	CWNGOPT
0.0	.27769	.01844	-.2733	.14335	CWNGNOT
-0.5	.25815	.01616	-.2582	.13363	CWNGNOT
-1.0	.23633	.01379	-.2399	.12250	CWNGNOT
-1.5	.21561	.01194	-.2235	.11216	CWNGNOT
-2.0	.19506	.01035	-.2074	.10147	CWNGNOT
-2.5	.17402	.00900	-.1908	.09088	CWNGNOT
-3.0	.15088	.00778	-.1715	.07826	CWNGNOT
-3.5	.12788	.00707	-.1528	.06670	CWNGNOT
-4.0	.10475	.00676	-.1342	.05445	CWNGNOT
0.0	.29344	.01730	-.2949	.15959	CWLTOLD
-0.5	.27181	.01488	-.2769	.14814	CWLTOLD
-1.0	.	.	.	.	CWLTOLD
-1.5	.22862	.01107	-.2415	.12477	CWLTOLD
-2.0	.20594	.00944	-.2224	.11267	CWLTOLD
-2.5	.18278	.00821	-.2031	.10011	CWLTOLD
-3.0	.16091	.00754	-.1857	.08840	CWLTOLD
-3.5	.13517	.00688	-.1632	.07429	CWLTOLD
-4.0	.11080	.00692	-.1430	.06096	CWLTOLD
1.0	.33443	.02268	-.3286	.18121	CWLTNEW
-0.5	.26995	.01472	-.2748	.14687	CWLTNEW
-1.0	.24789	.01259	-.2564	.13492	CWLTNEW
-1.5	.22561	.01084	-.2379	.12261	CWLTNEW
-2.0	.20356	.00937	-.2197	.11107	CWLTNEW
-2.5	.18022	.00831	-.2006	.09806	CWLTNEW
-3.0	.15831	.00754	-.1826	.08659	CWLTNEW
-3.5	.13301	.00701	-.1608	.07264	CWLTNEW
-4.0	.10839	.00712	-.1403	.05918	CWLTNEW

Table 4. WIBCO-PPW Predicted Percentage Drag Reductions Due to Winglets at M = 0.8 Using a = 0.8 Chord Loading

	C_L = 0.18	C_L = 0.22	C_L = 0.26
CASE F	18%	16%	12.7%
CASE G	14.8%	14.6%	12.7%
CROPPED DELTA G	14.7%	15.4%	13.3%

Table 5. Predicted Upper Surface Boundary Layer Separation Locations Versus Iterations for Modified Cropped Delta G Wing-Winglet at M = 0.8, α = -0.5° (150 crude grid iterations)

x/c for Boundary Layer Separation

η	154 its	214 its	254 its	314 its	354 its	414 its
.145	.985					
.195	.983					
.245	.983					
.295	.979					
.347	.980					
.400	.978					
.455	.972					
.511	.969					
.570	.967		.999			.996
.631	.965					
.695	.963		.972			
.763	.960		.957	.997	.978	.990
.836	.955	.979	.955	.976	.948	.979
.914	.956	.952	.951	.951	.947	.957

Table 5. (Concluded) - Predicted Upper Surface Boundary Layer Separation Locations Versus Iterations for Cropped Delta G Optimum Wing-Alone at M = 0.8, α = -0.5° (150 crude grid iterations)

x/c for Boundary Layer Separation

η	154 its	214 its	254 its	314 its	354 its	414 its	450 its
.139	.984						
.186	.982						
.234	.980						
.282	.975						
.332	.976						.996
.382	.973			.995		.994	
.435	.968			.993		.990	
.488	.967			.990		.996	
.544	.962			.985	.988		
.603	.955		.965	.990	.996	.990	
.665	.951		.959	.990	.995	.987	
.730	.945	.997		.990	.994	.985	1.000
.799	.942	.992		.987		.991	.993
.874	.940	.988	.996		.997	.992	.994
.956	.951				.998		

Table 6. Shock-Induced Trailing Edge Boundary Layer Separation Prediction Using Method of Ref. 11

Configuration	$(x/c)_{crest}$	(c/R)	δ_{tel}(rad)	δ_{tec}(rad)	α_t(rad)	α_{ted}
Crop Delta G w-wlt	0.4	.4584	.02761	.09299	.0494	-3.509°
Crop Delta G wing	0.4	.4812	.04157	.10671	.0512	-4.309°
G w-wlt	0.4	.4583	.02770	.09307	.0502	-3.555°
G wing	0.4	.4817	.04183	.10695	.0522	-4.380°
F w-wlt	0.4	.4404	.02522	.09058	.0534	-1.758°
F wing	0.4	.4676	.03887	.10394	.0578	-2.674°

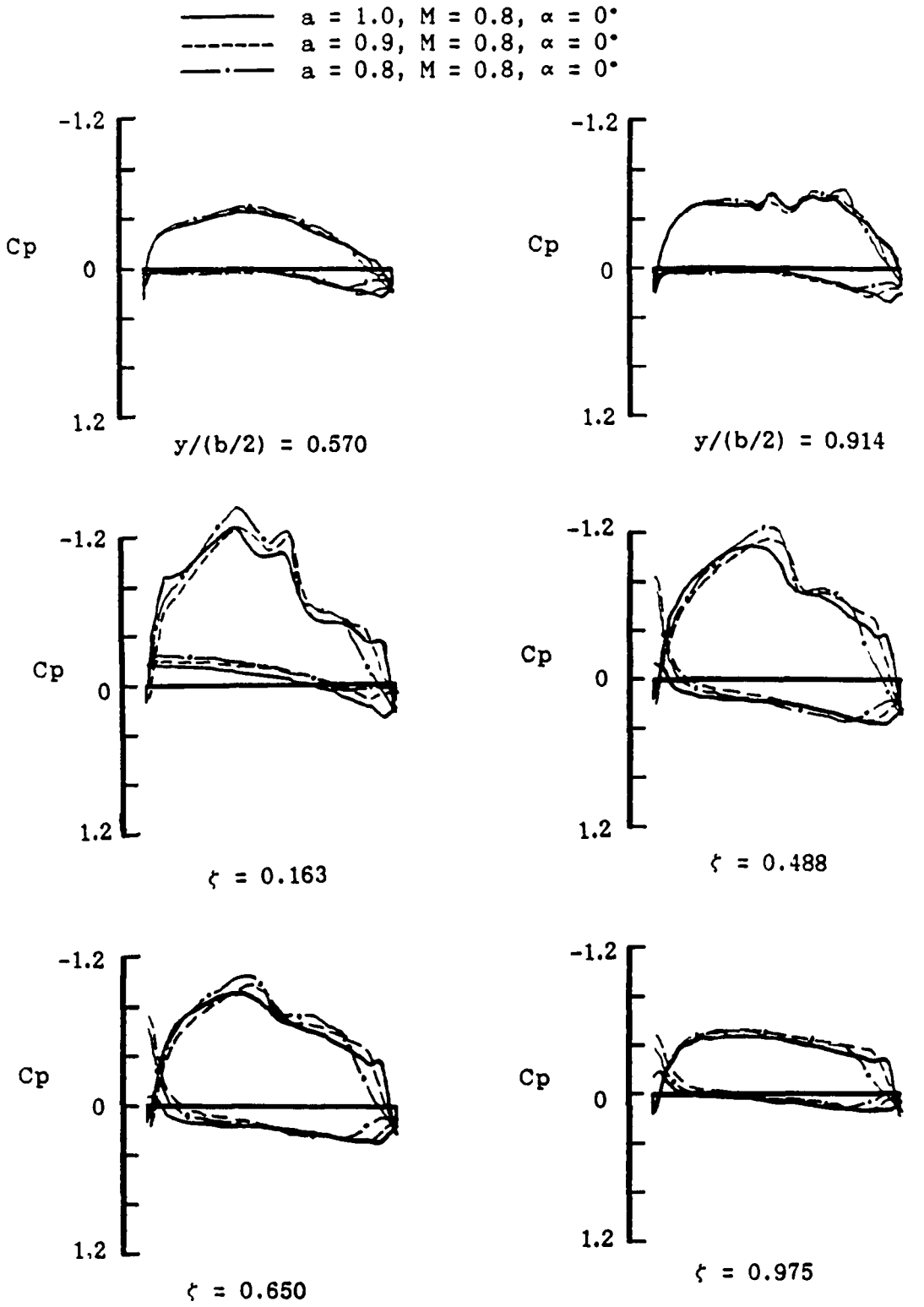

Fig. 1 Calculated wing-winglet C_p distributions for configuration F at M = 0.8, $C_L \approx 0.27$, for various chord loading shape functions, from ref. 3.

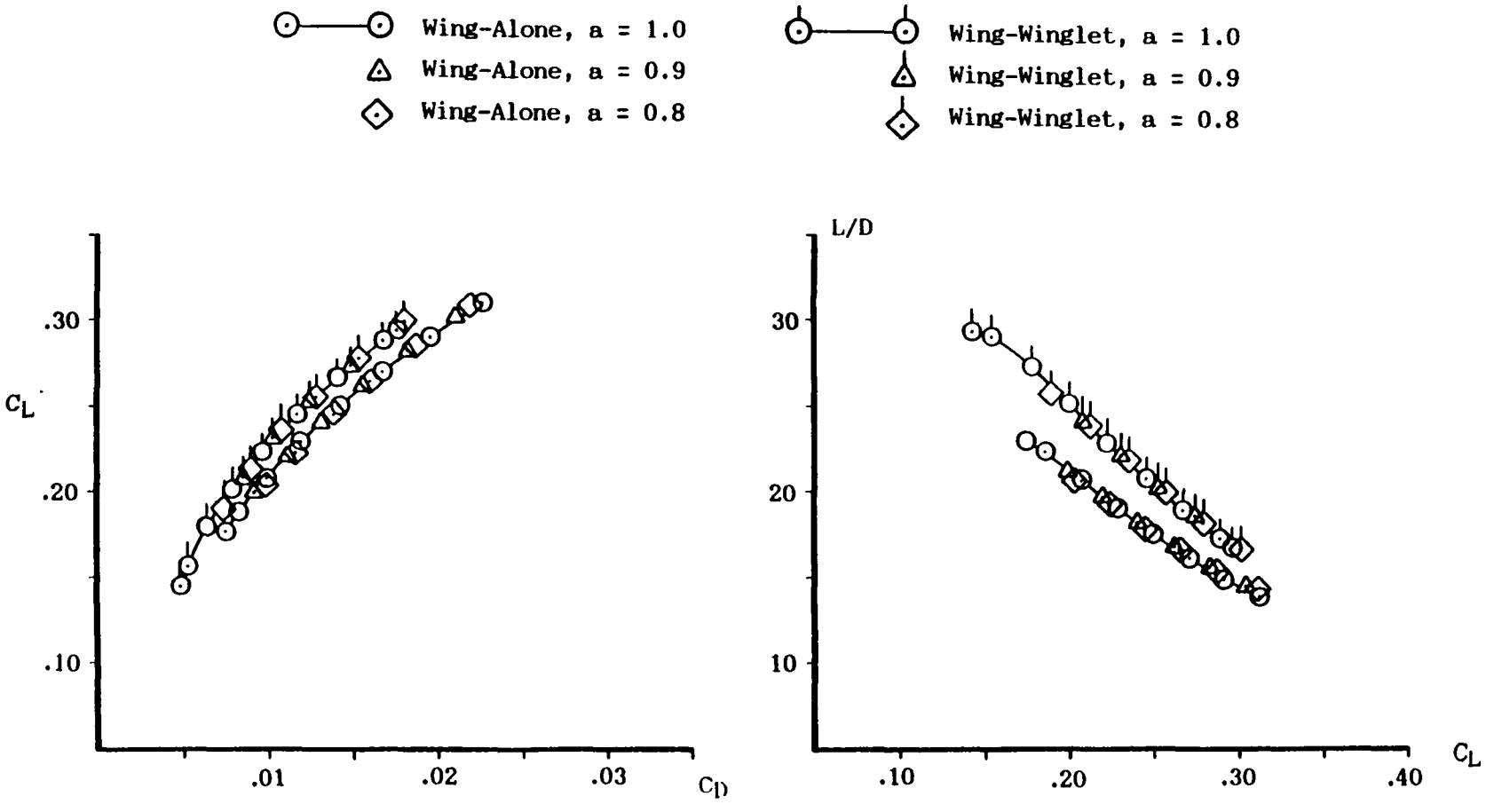

Fig. 2 Predicted performance of wing-alone and wing-winglet configurations F at M = 0.8, for various chord loading shape functions, from ref. 3.

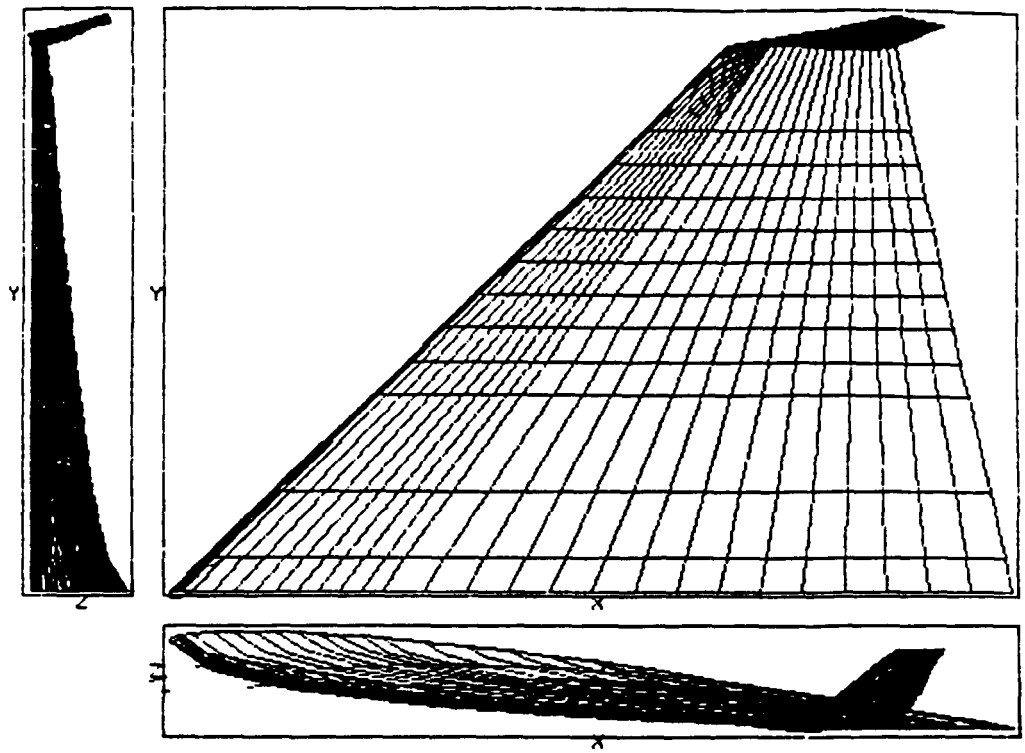

Fig. 3 Wing-winglet geometry for configuration F (A = 2.20, Λ = 45°, λ = 0.2).

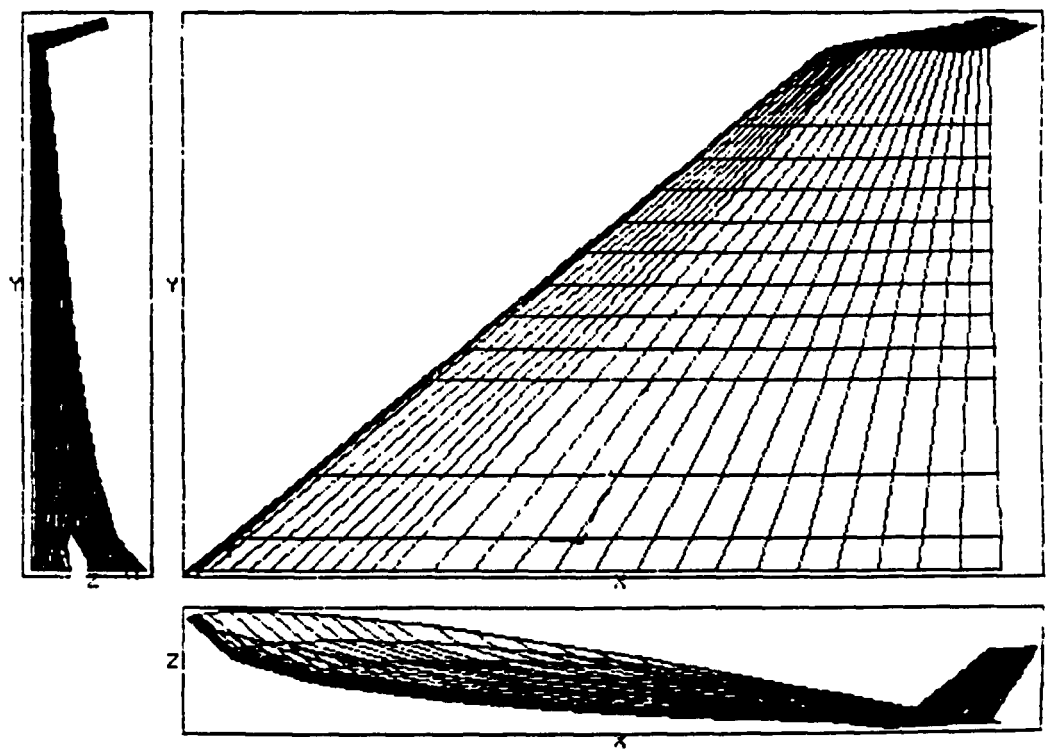

Fig. 4 Wing-winglet geometry for configuration G (A = 2.20, Λ = 50°, λ = 0.2).

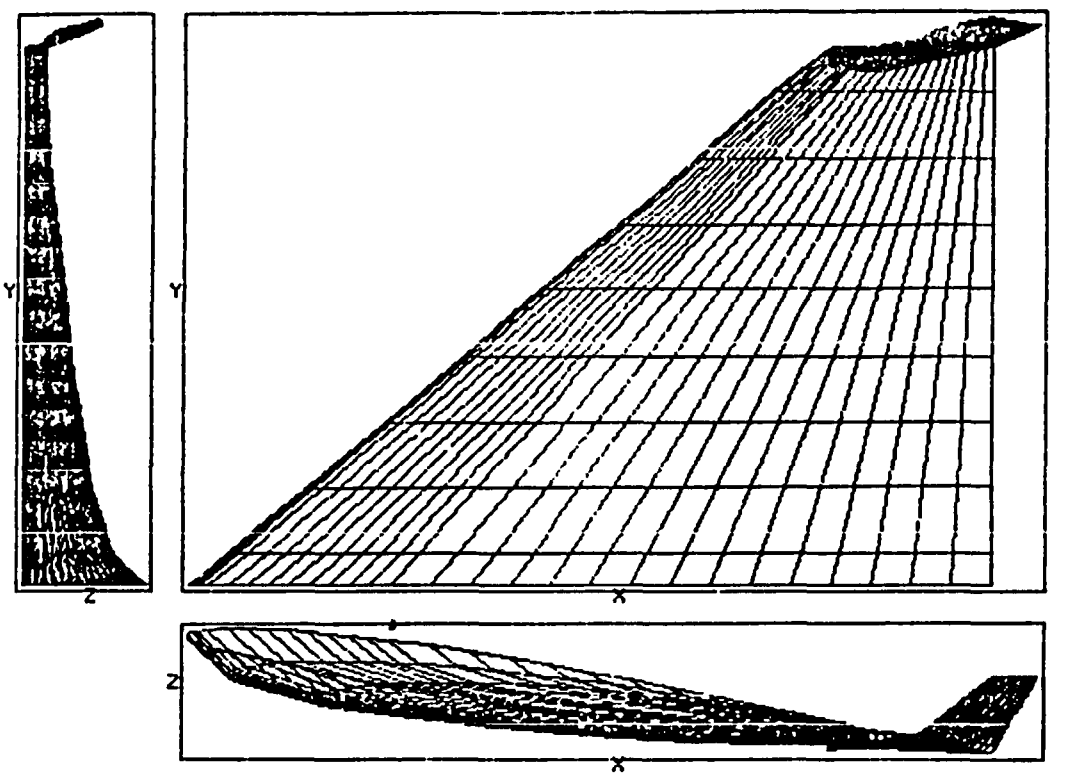

Fig. 5. Wing-winglet geometry for configuration cropped delta G (A = 2.22, Λ = 50°, λ = 0.203).

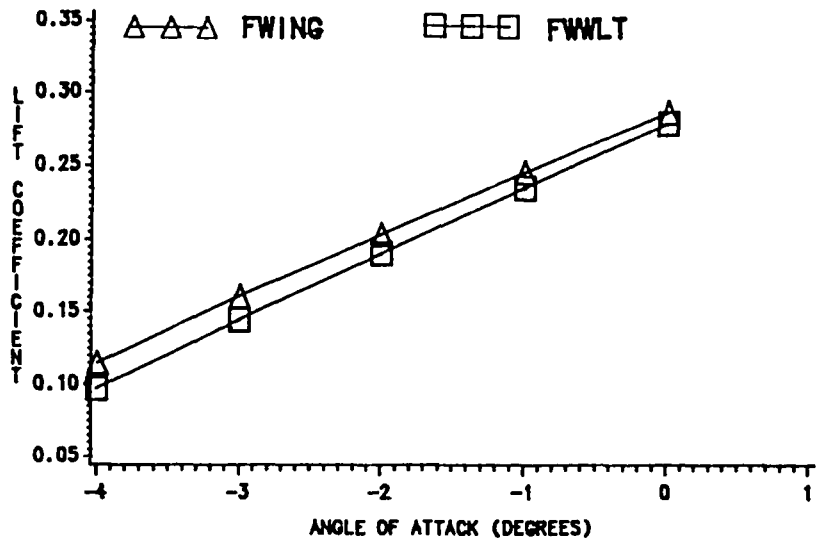

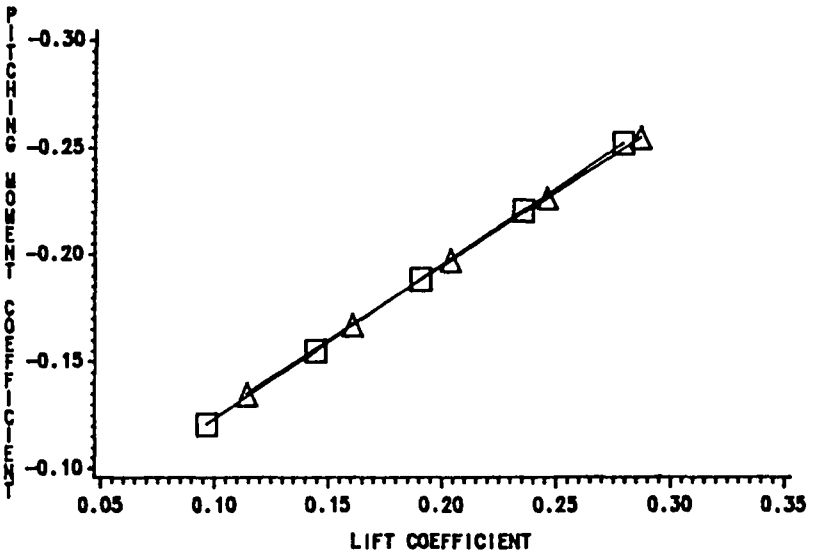

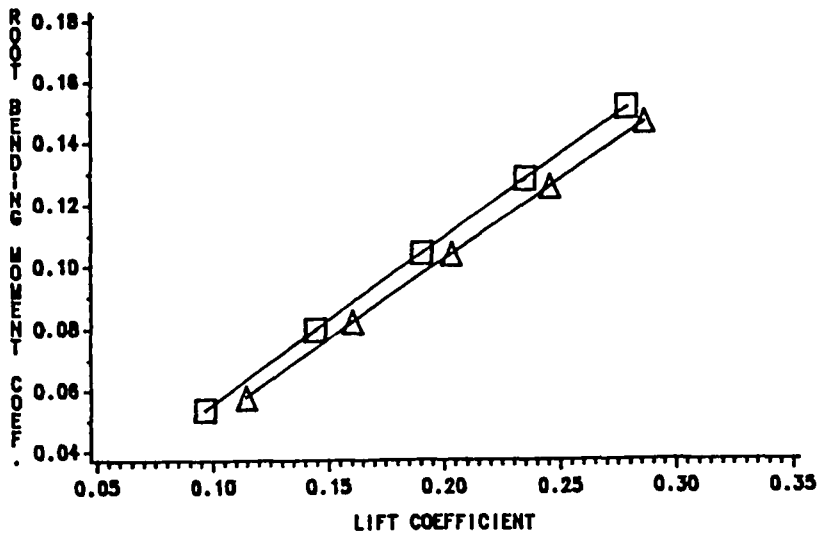

Fig. 6. Predicted performance of wing-alone and wing-winglet configurations F at M = 0.8; C_L - α, C_m - C_L, C_B - C_L.

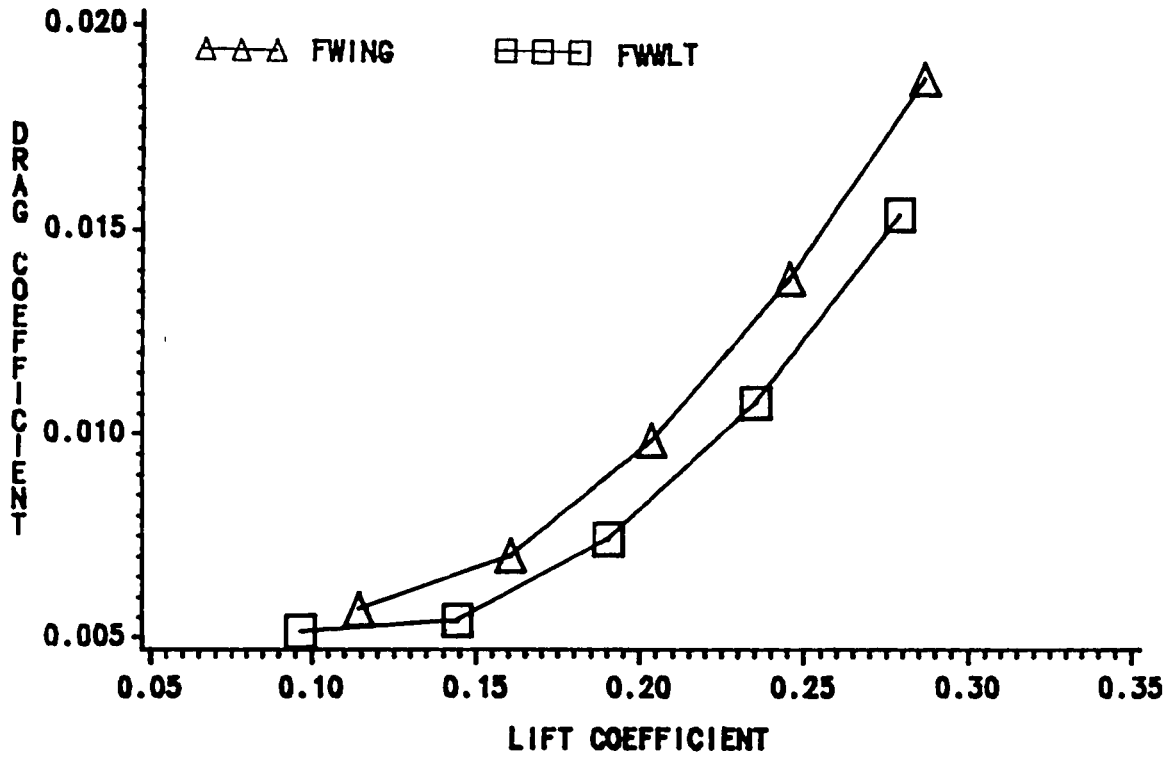

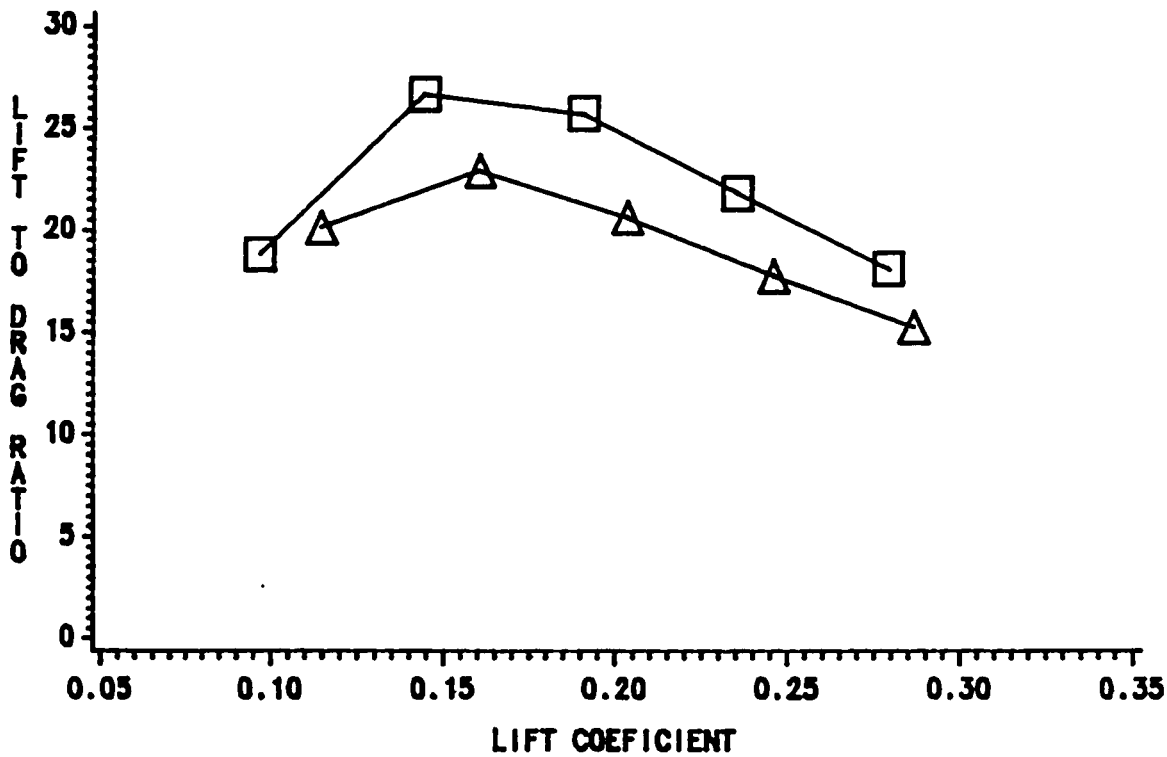

Fig. 6. (Concluded) - Predicted performance of wing-alone and wing-winglet configurations F at M = 0.8; drag polar and L/D - C_L.

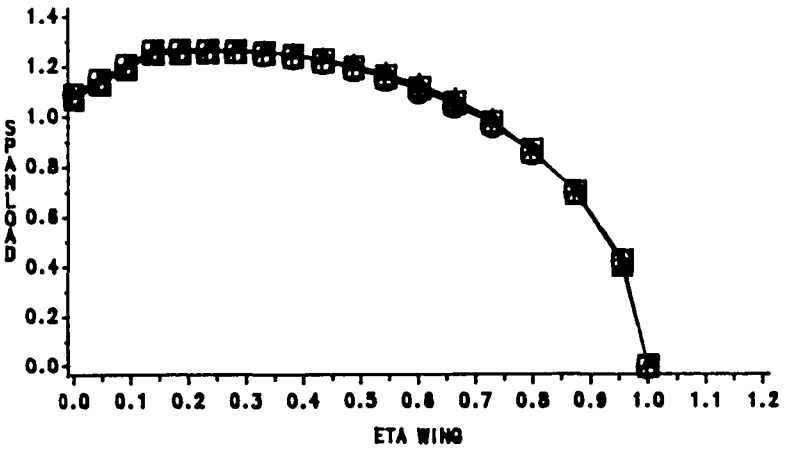

DIAMOND: A=1 TRIANGLE: A=-2
CIRCLE: A=0 SQUARE: A=-4

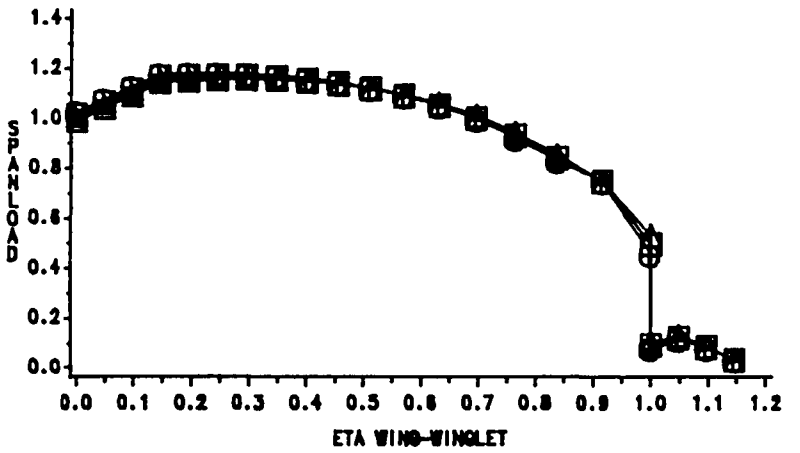

Fig. 7. Calculated normalized spanloads for wing-alone and wing-winglet configurations F at M = 0.8.

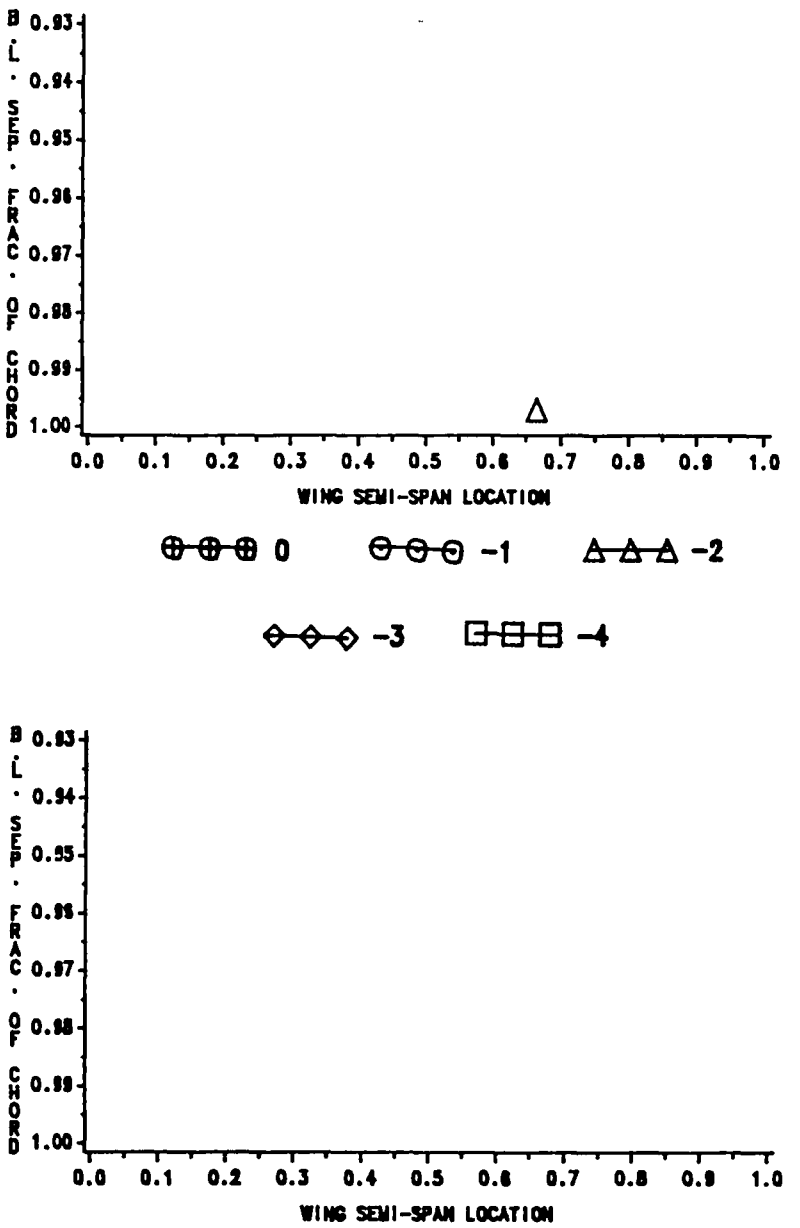

Fig. 8. Predicted upper surface boundary layer separation locations for wing-alone and wing-winglet configurations F at M = 0.8.

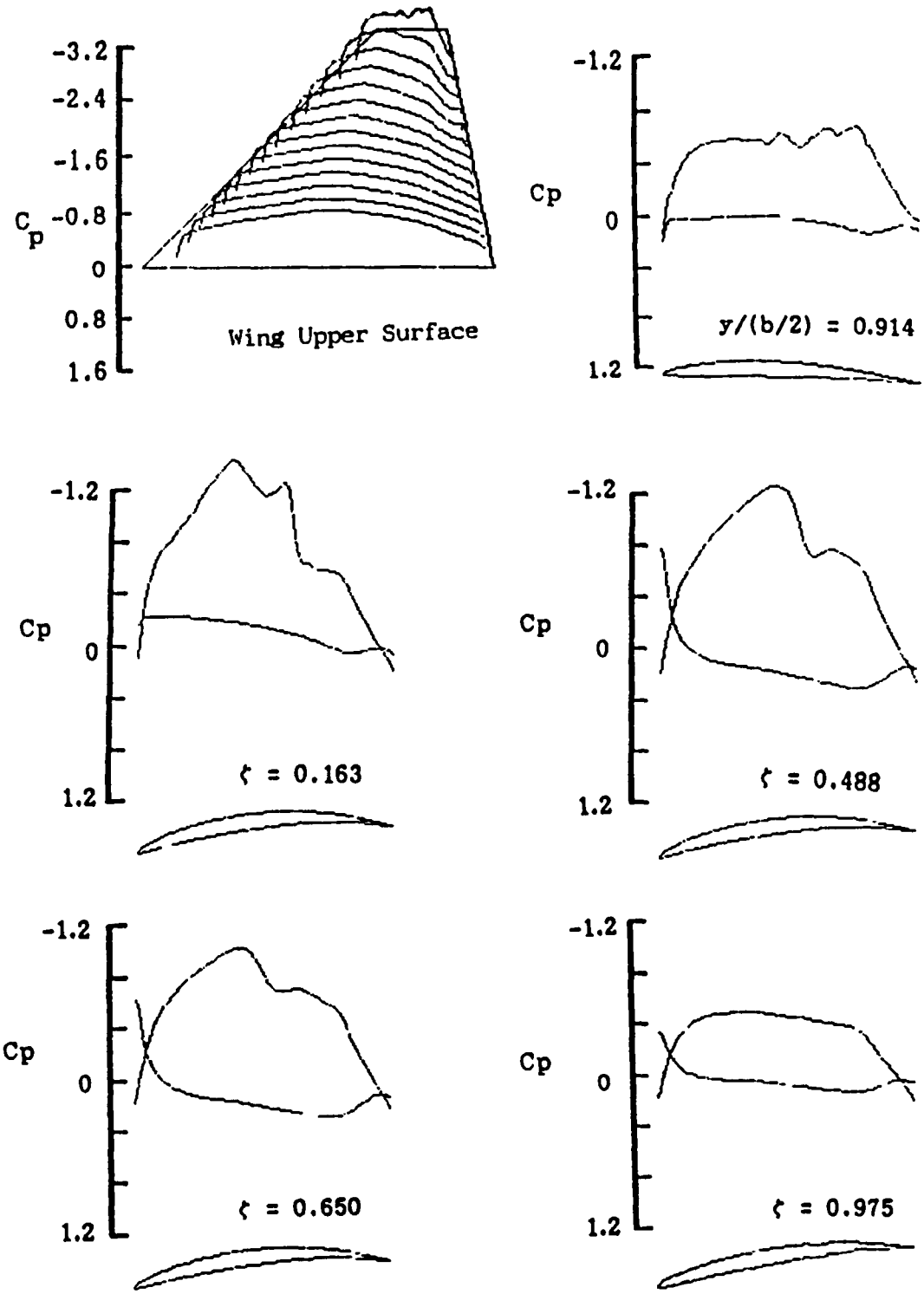

Fig. 9. Calculated wing-winglet C_p distributions for configuration F at M = 0.8, $\alpha = 0°$.

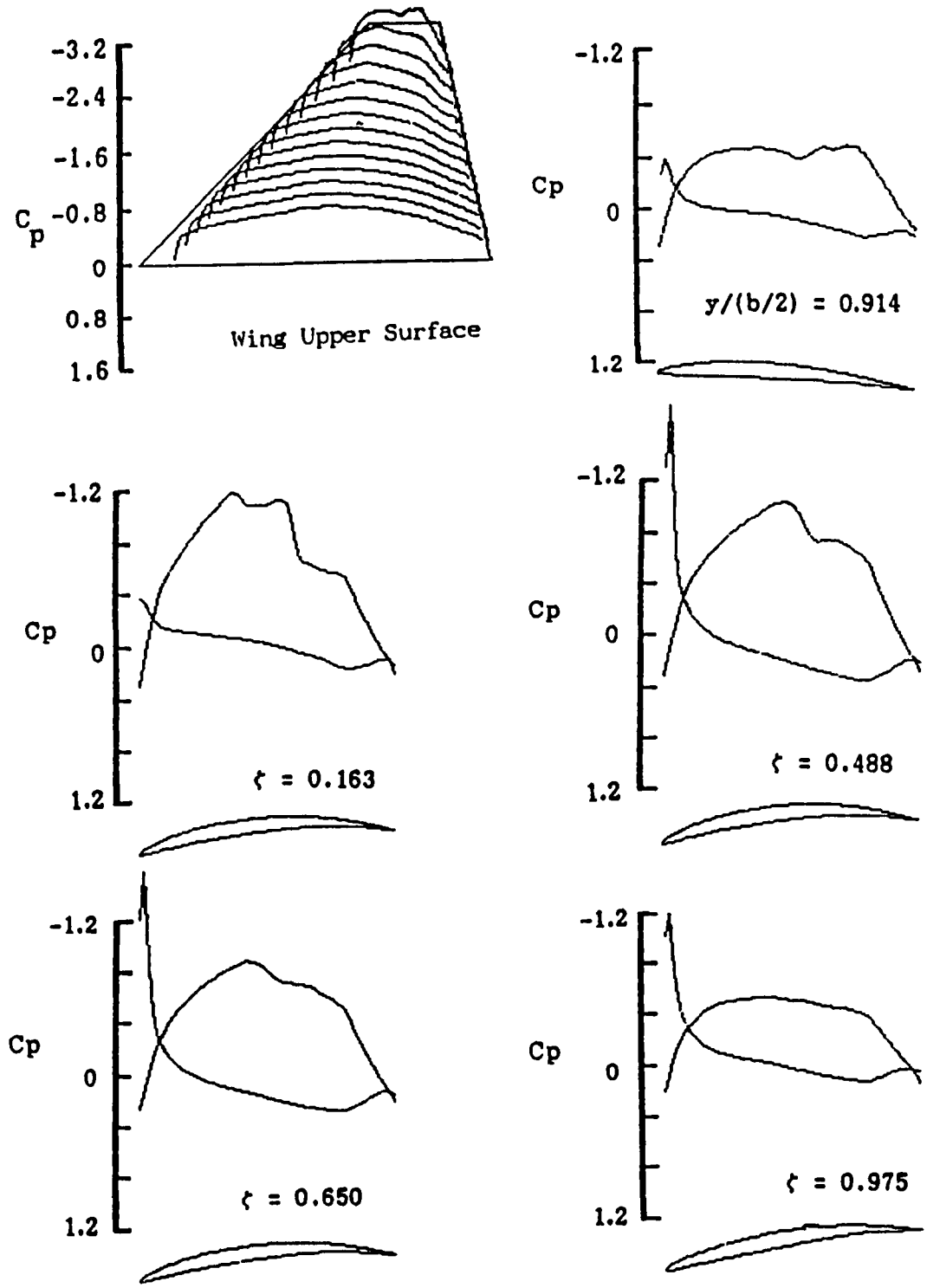

Fig. 10. Calculated wing-winglet C_p distributions for configuration F at M = 0.8, α = -1.5°.

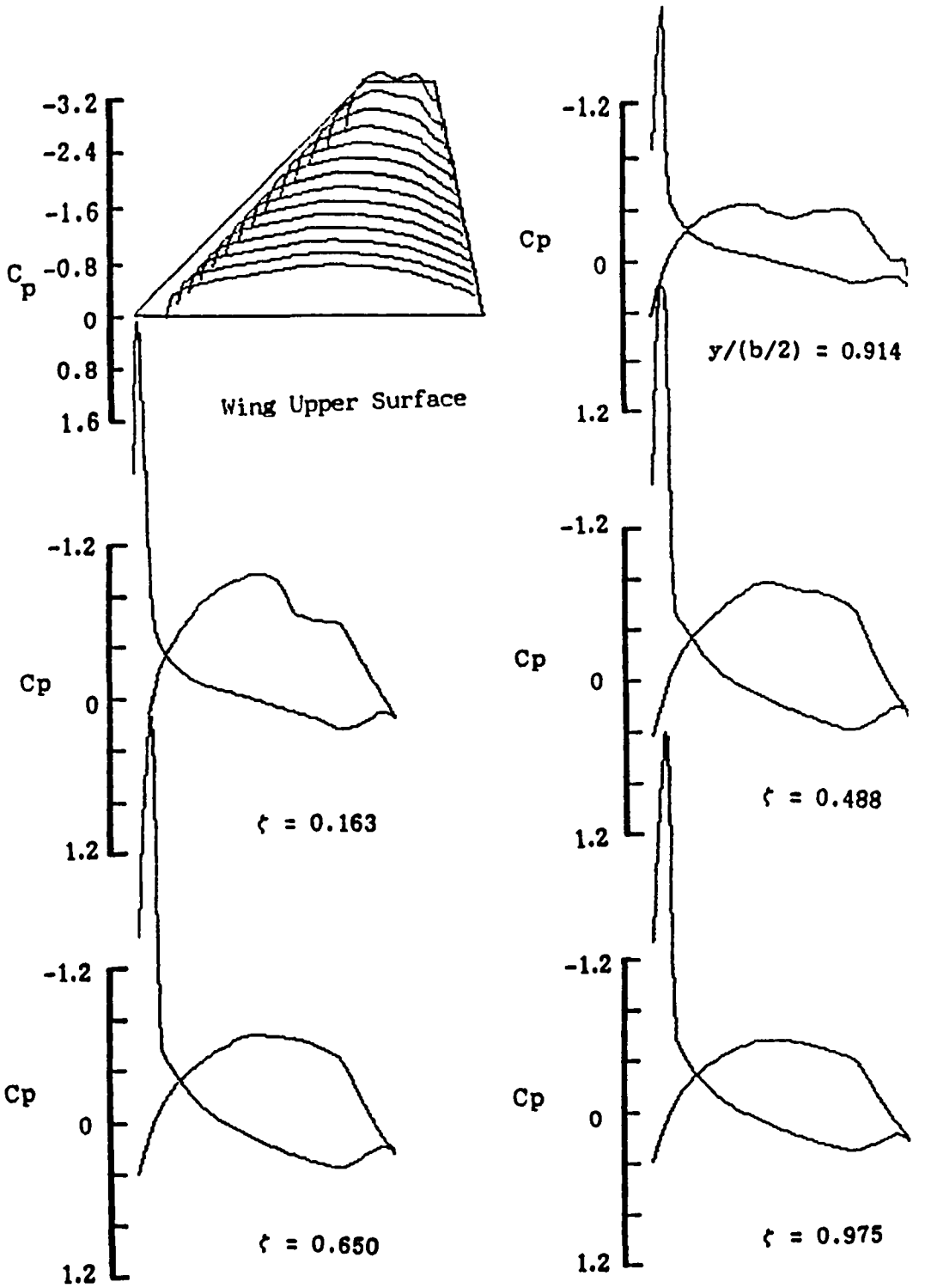

Fig. 11. Calculated wing-winglet C_p distributions for configuration F at M = 0.8, $\alpha = -4°$.

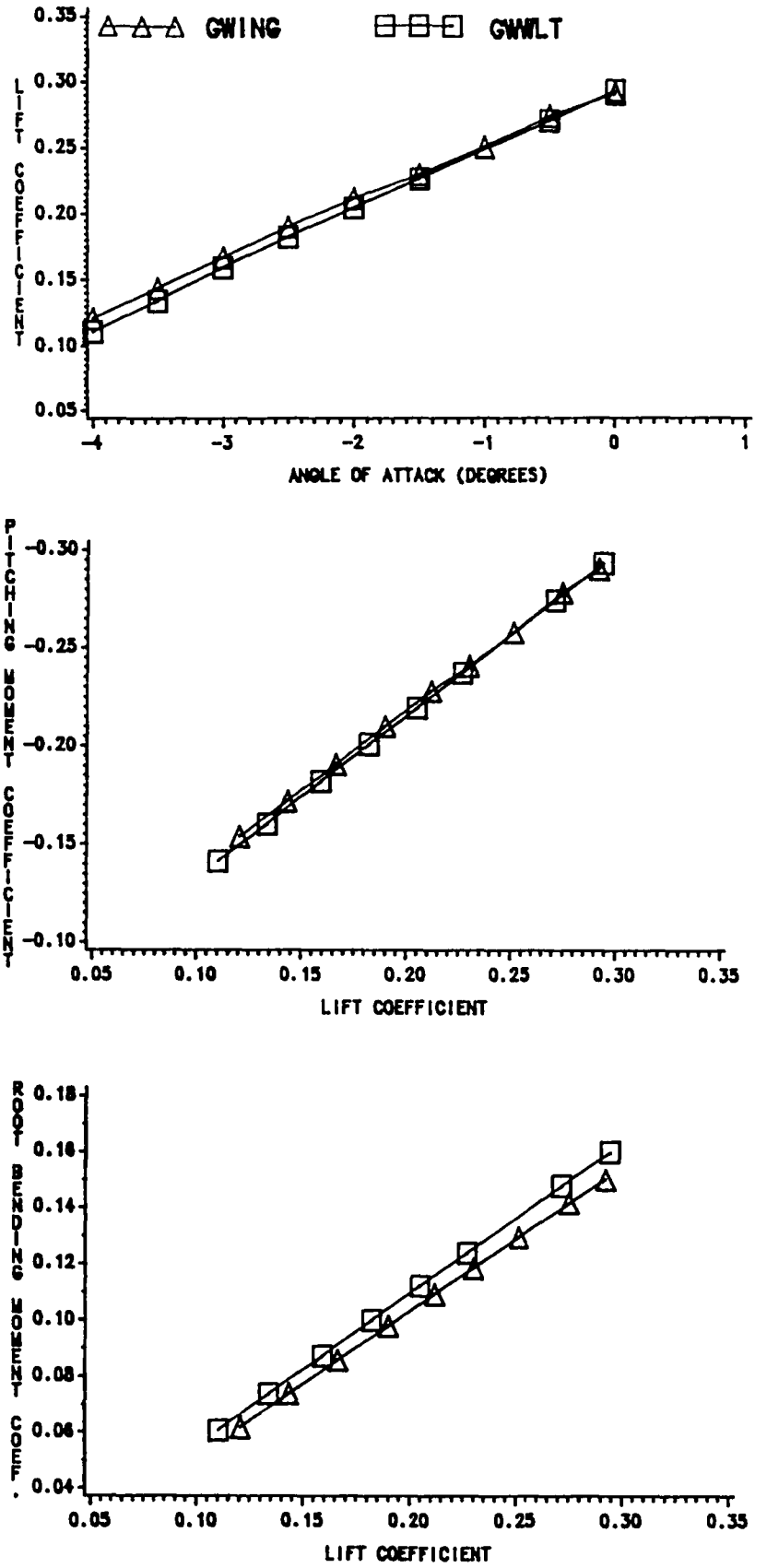

Fig. 12. Predicted performance of wing-alone and wing-winglet configurations G at M = 0.8; C_L - α, C_m - C_L, C_B - C_L.

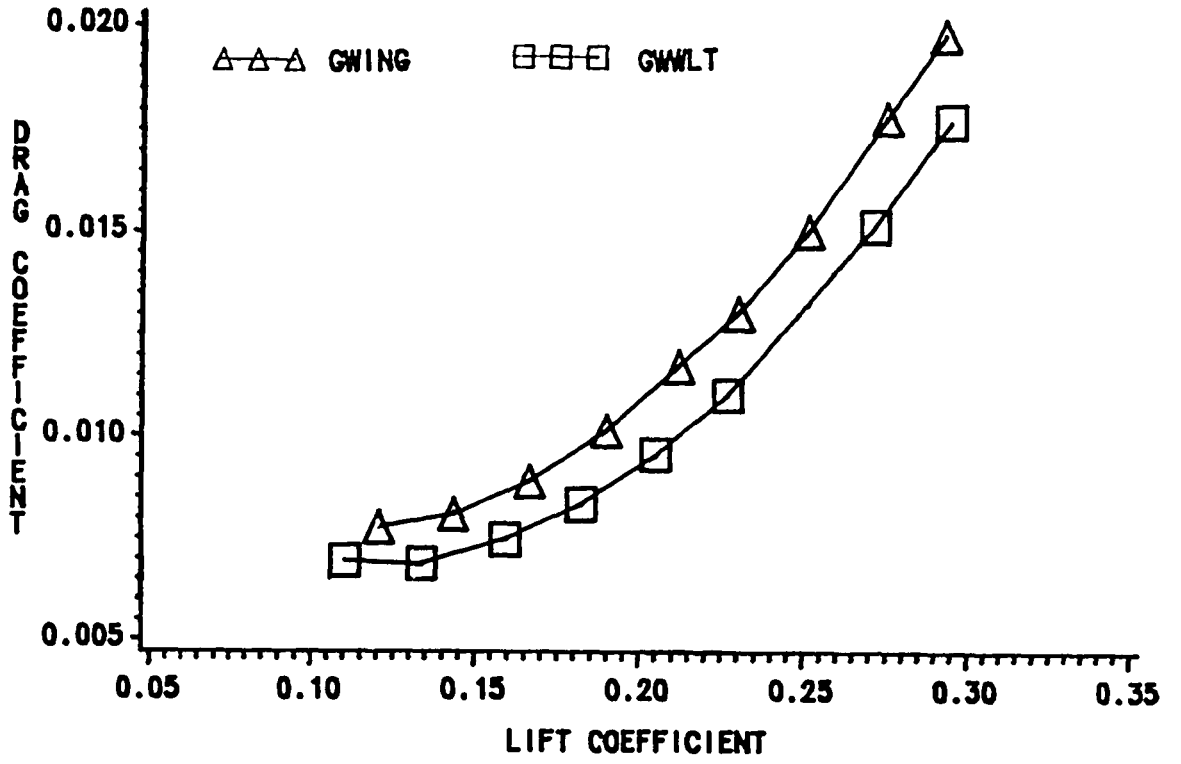

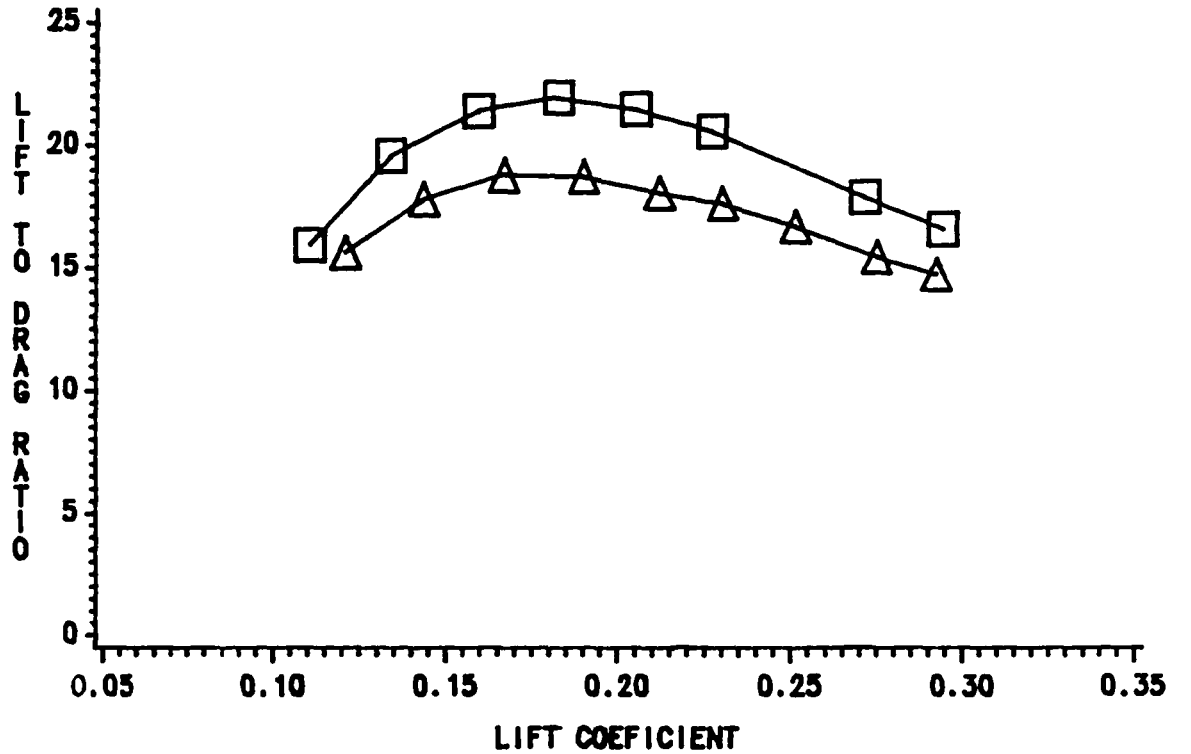

Fig. 12. (Concluded) – Predicted performance of wing-wlone and wing-winglet configurations G at M = 0.8; drag polar and L/D - C_L.

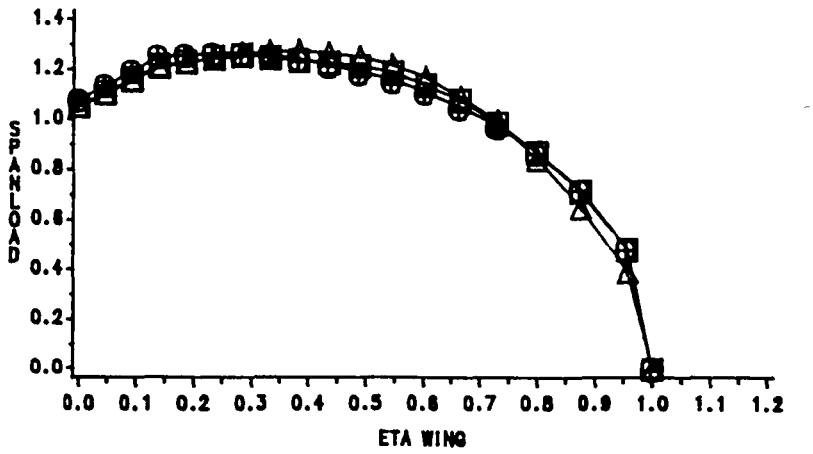

DIAMOND: A=1 TRIANGLE: A=2
CIRCLE: A=0 SQUARE: A=4

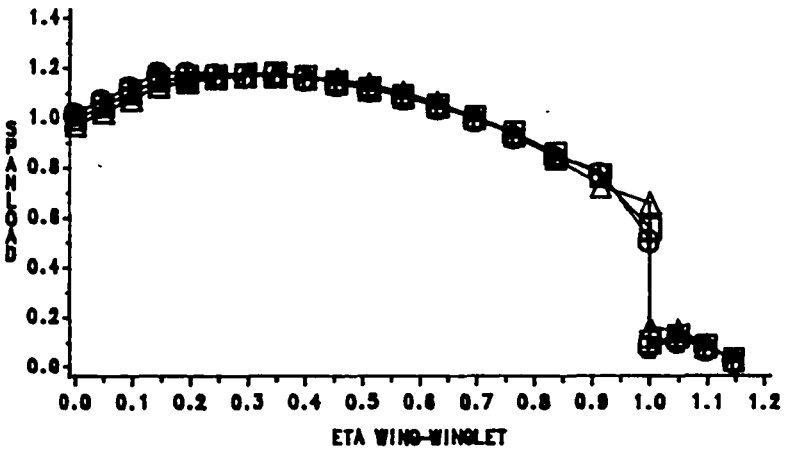

Fig. 13. Calculated normalized spanloads for wing-alone and wing-winglet configurations G at M = 0.8.

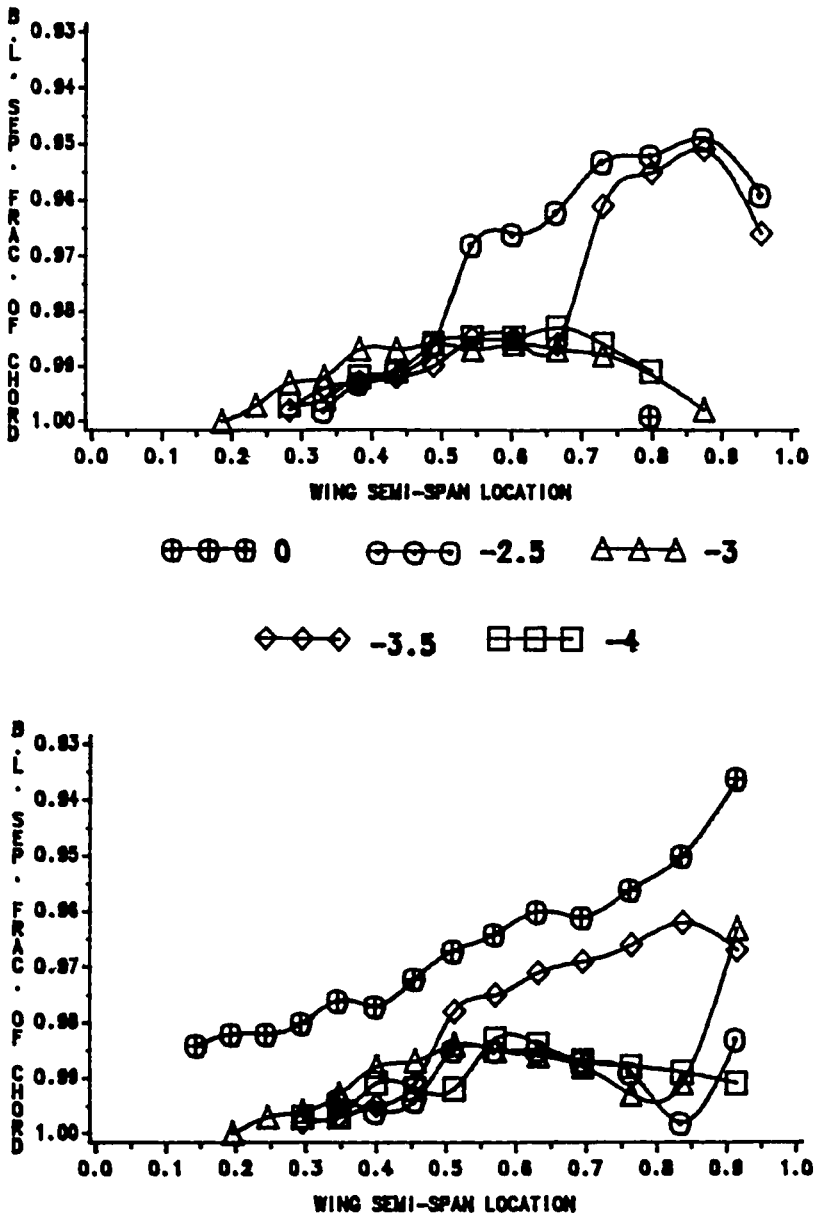

Fig. 14. Predicted upper surface boundary layer separation locations for wing-alone and wing-winglet configurations G at M = 0.8.

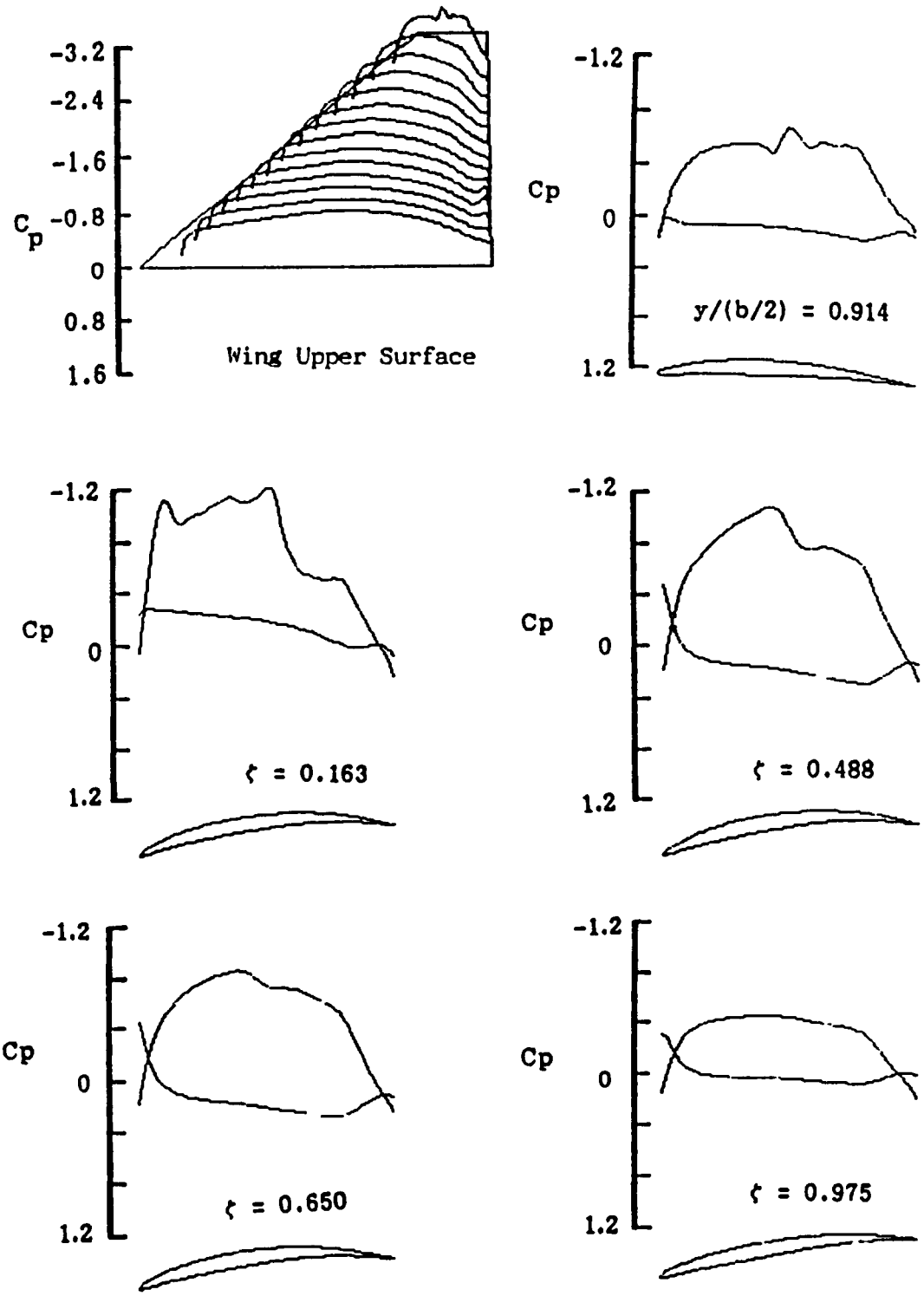

Fig. 15. Calculated wing-winglet C_p distributions for configuration G at M = 0.8, α = 0°.

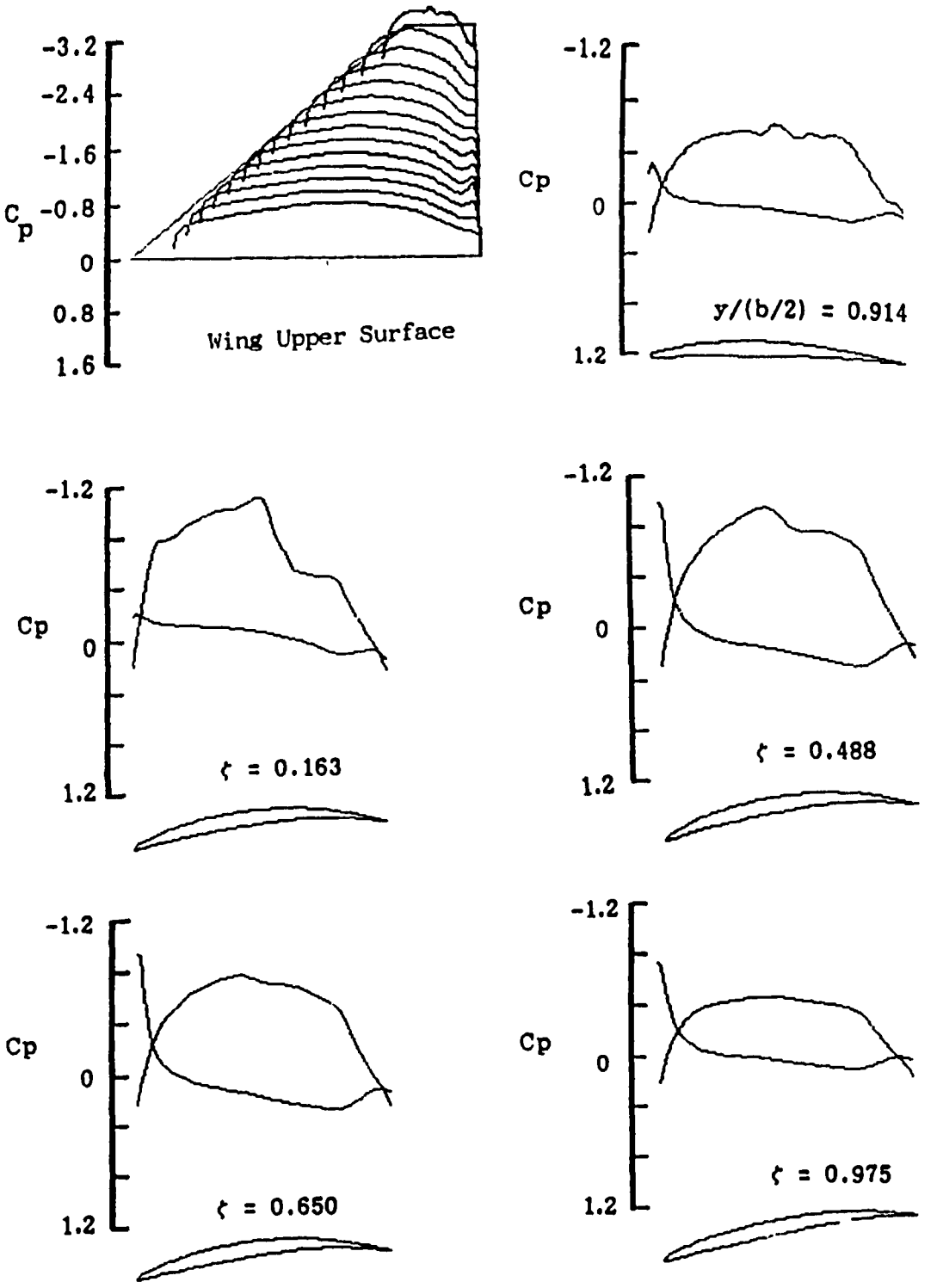

Fig. 16. Calculated wing-winglet C_p distributions for configuration G at M = 0.8, α = -1.5°.

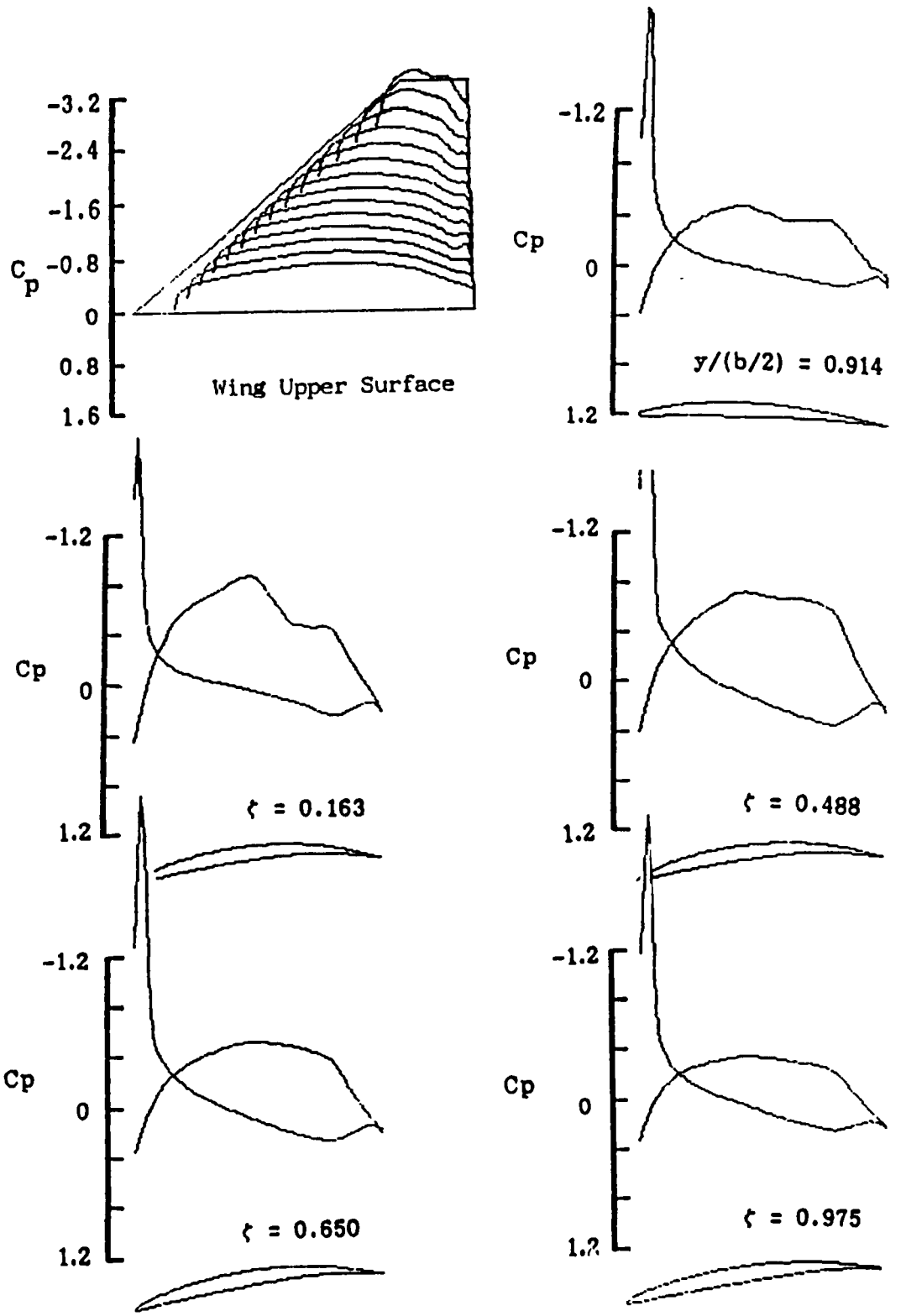

Fig. 17. Calculated wing-winglet C_p distributions for configuration G at M = 0.8, α = -4°.

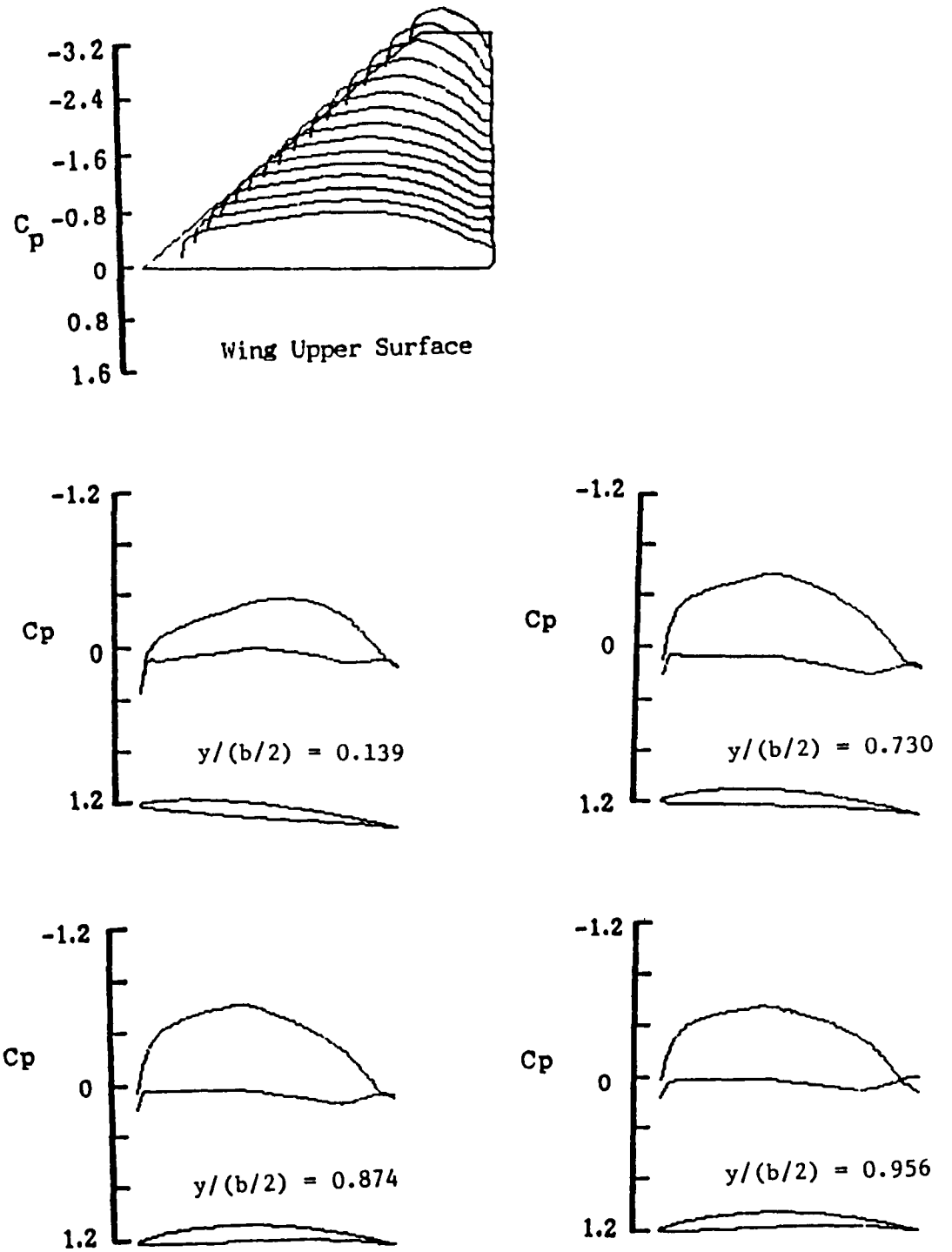

Fig. 18. Calculated wing-alone C_p distributions for configuration G at M = 0.8, $\alpha = 0°$.

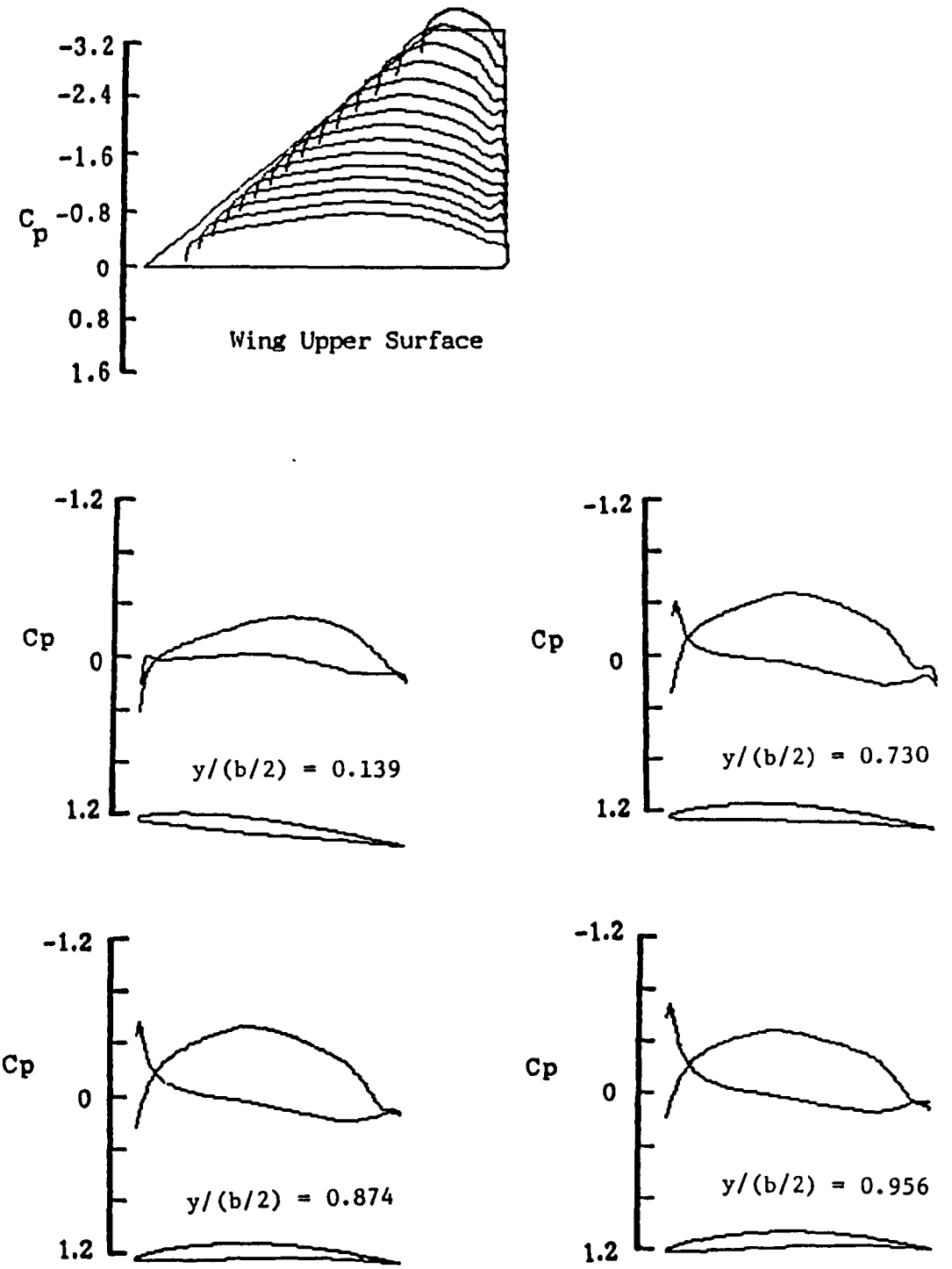

Fig. 19. Calculated wing-alone C_p distributions for configuration G at M = 0.8, $\alpha = -2°$.

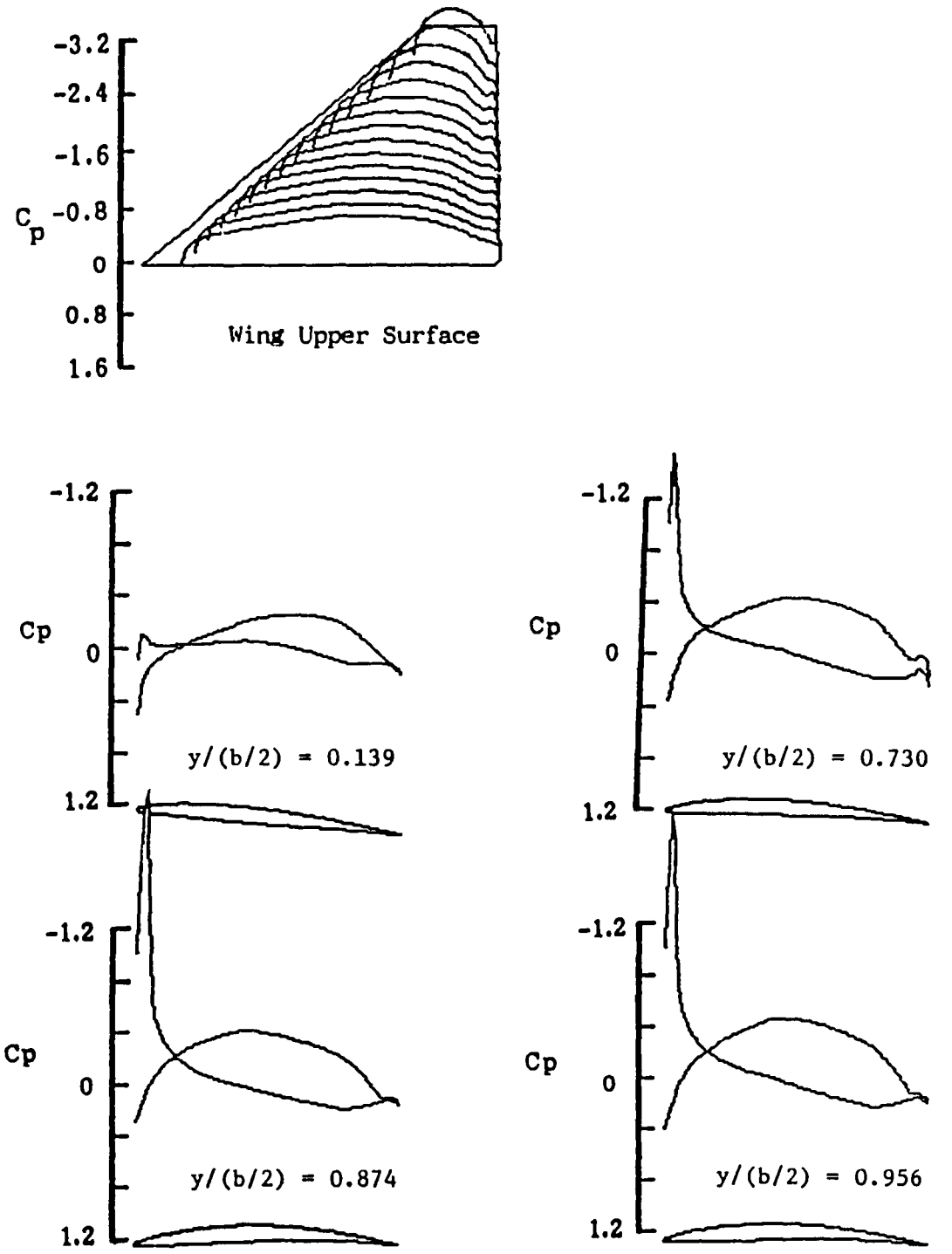

Fig. 20. Calculated wing-alone C_p distributions for configuration G at M = 0.8, $\alpha = -4°$.

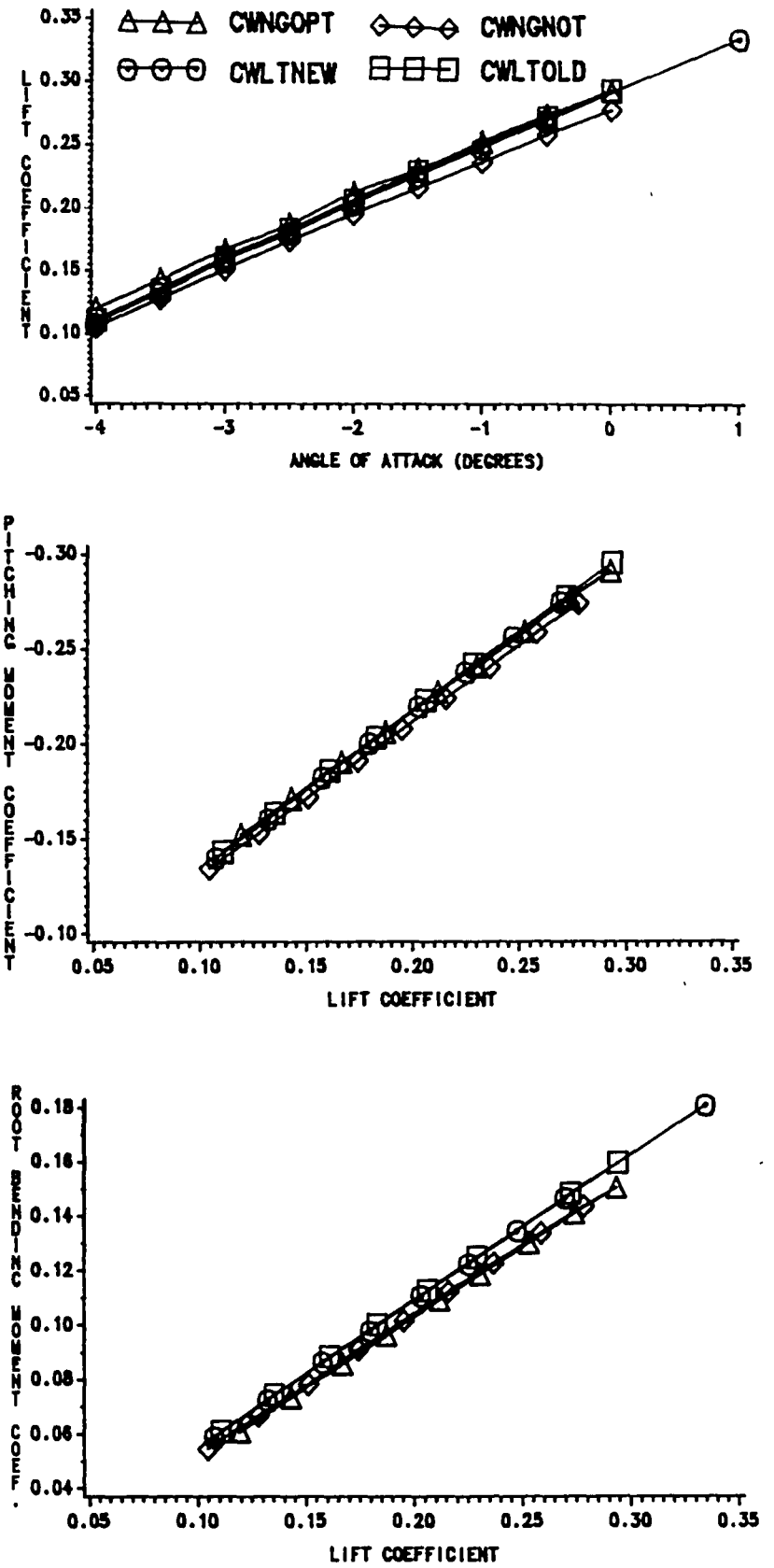

Fig. 21. Predicted performance of wing-alone and wing-winglet configurations cropped delta G at M = 0.8; C_L - α, C_m - C_L, C_B - C_L.

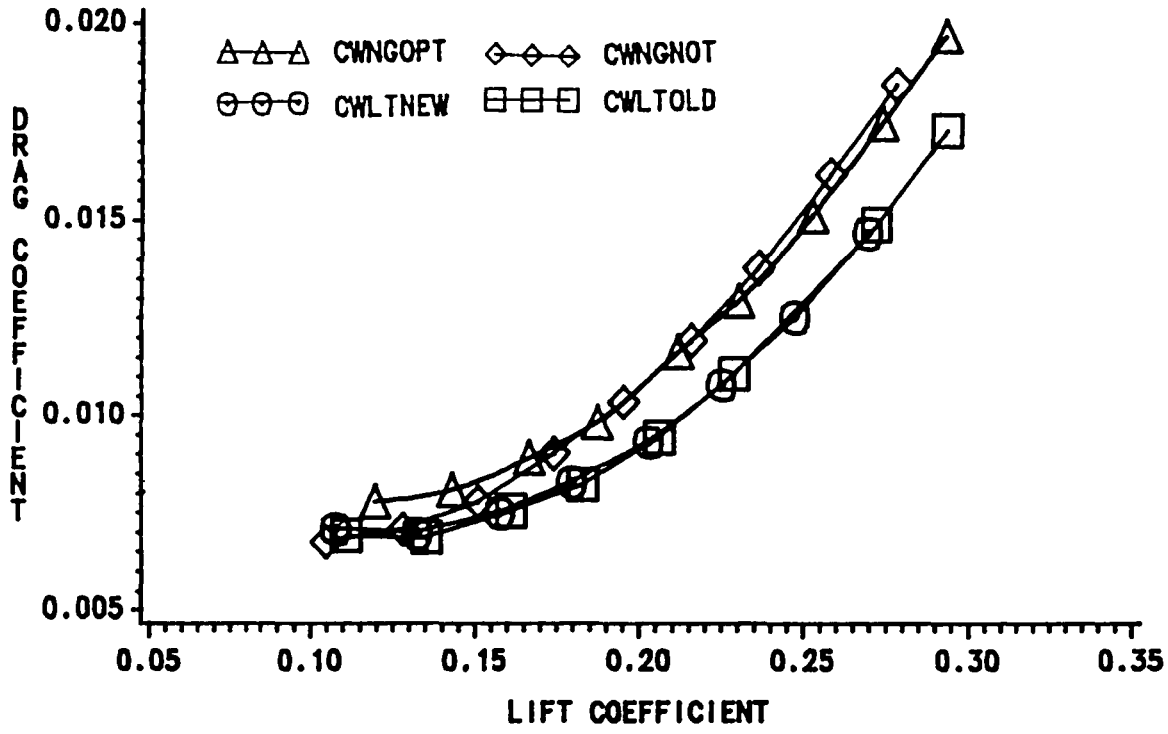

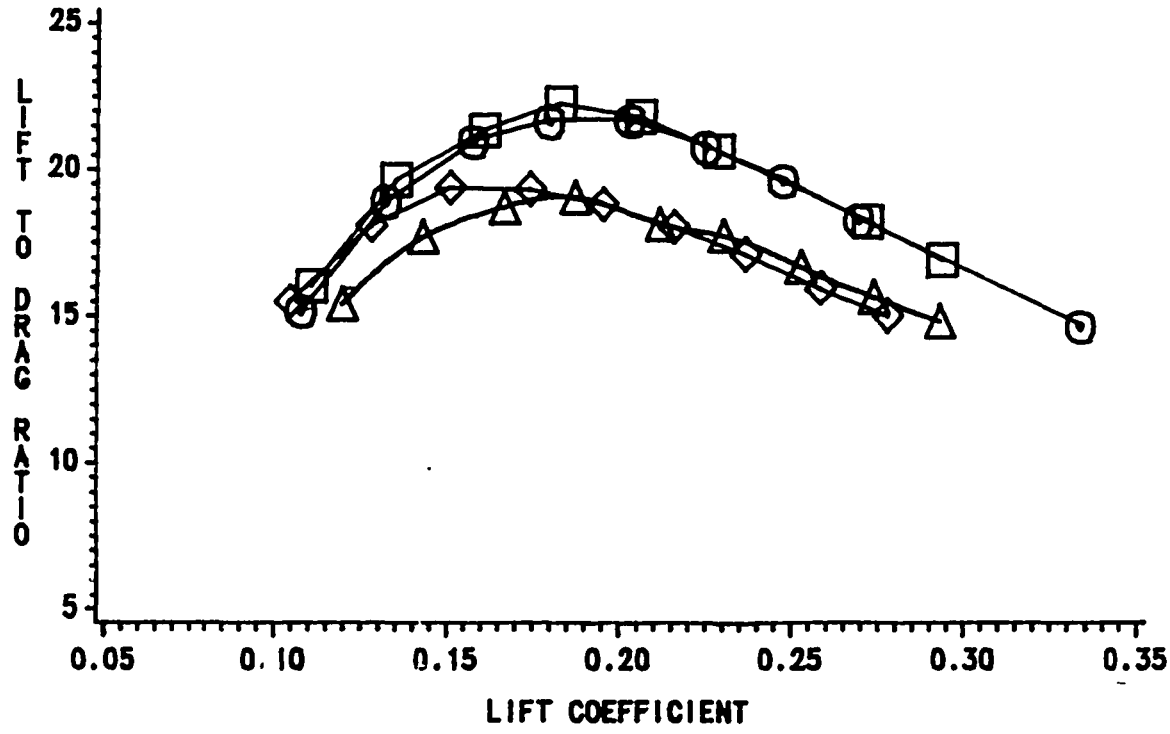

Fig. 21. (Concluded) - Predicted performance of wing-alone and wing-winglet configurations cropped delta G at M = 0.8; drag polar and L/D - C_L.

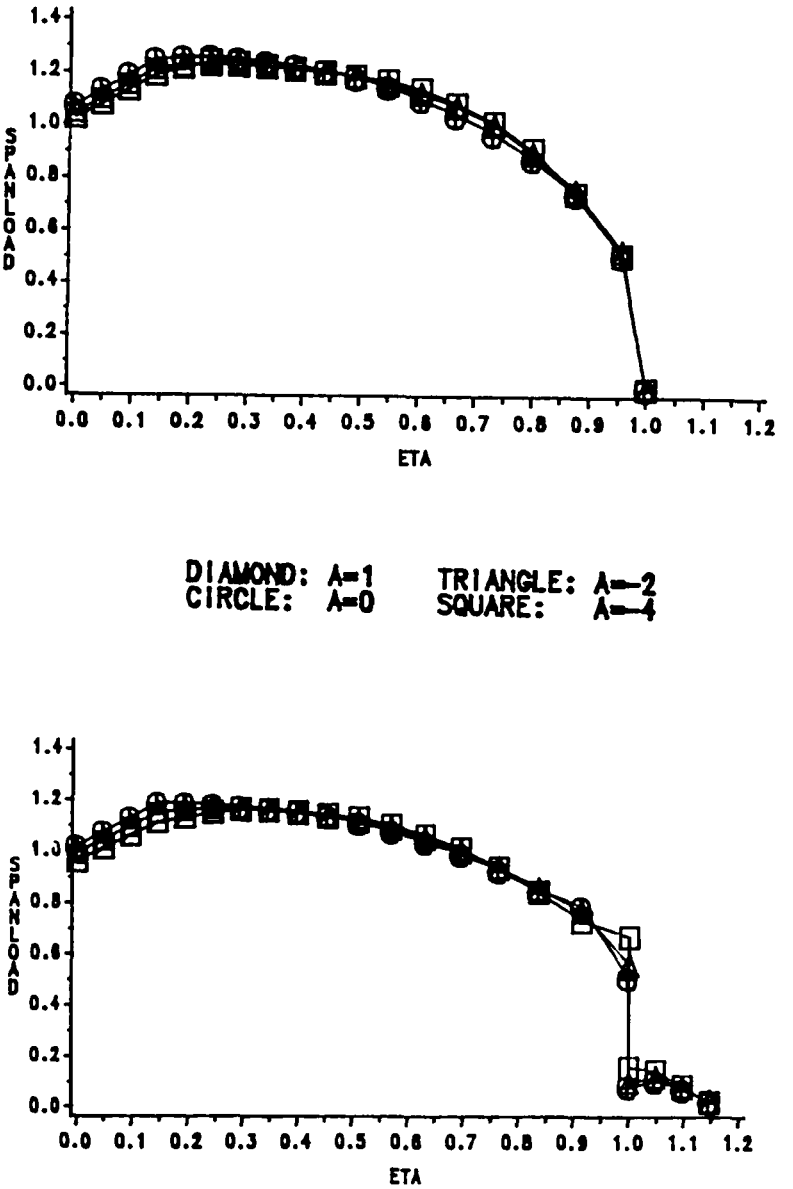

Fig. 22. Calculated normalized spanloads for wing-alone and wing-winglet configurations cropped delta G, wing of wing-winglet and wing-winglet at M = 0.8.

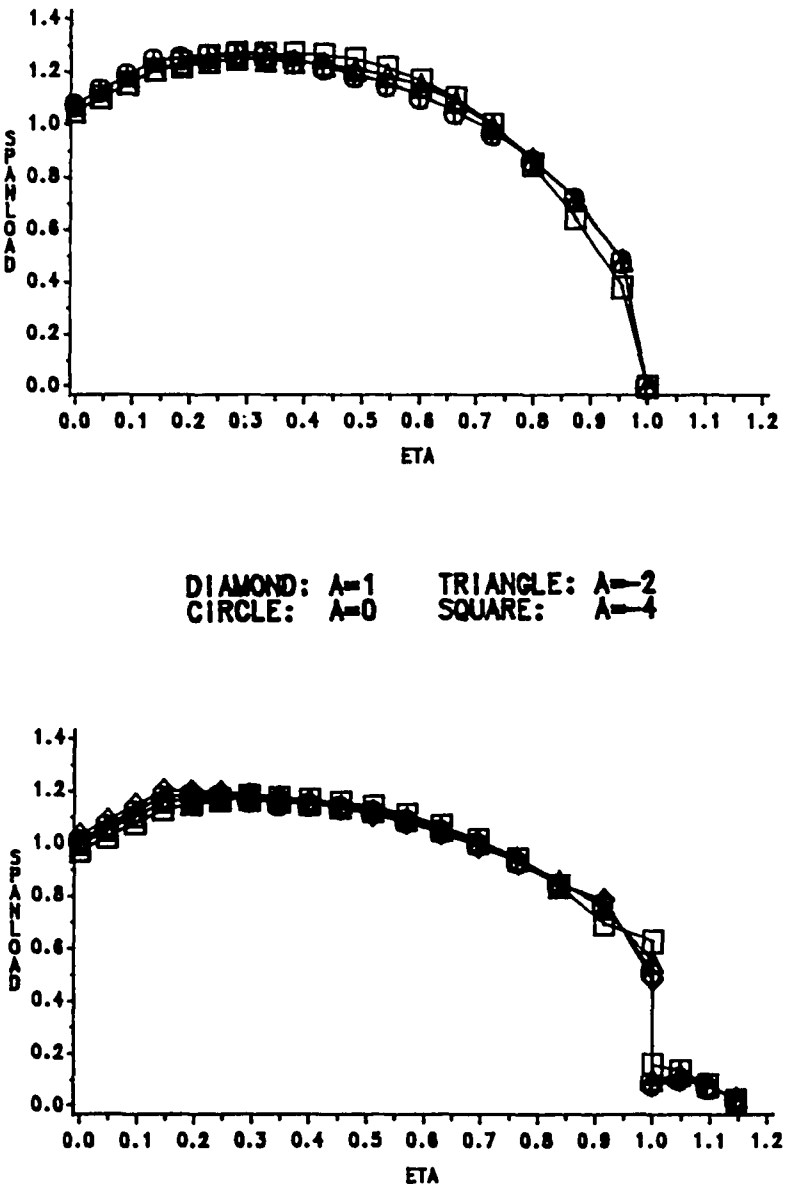

Fig. 23. Calculated normalized spanloads for wing-alone and wing-winglet configurations cropped delta G, optimum wing and modified wing-winglet at M = 0.8.

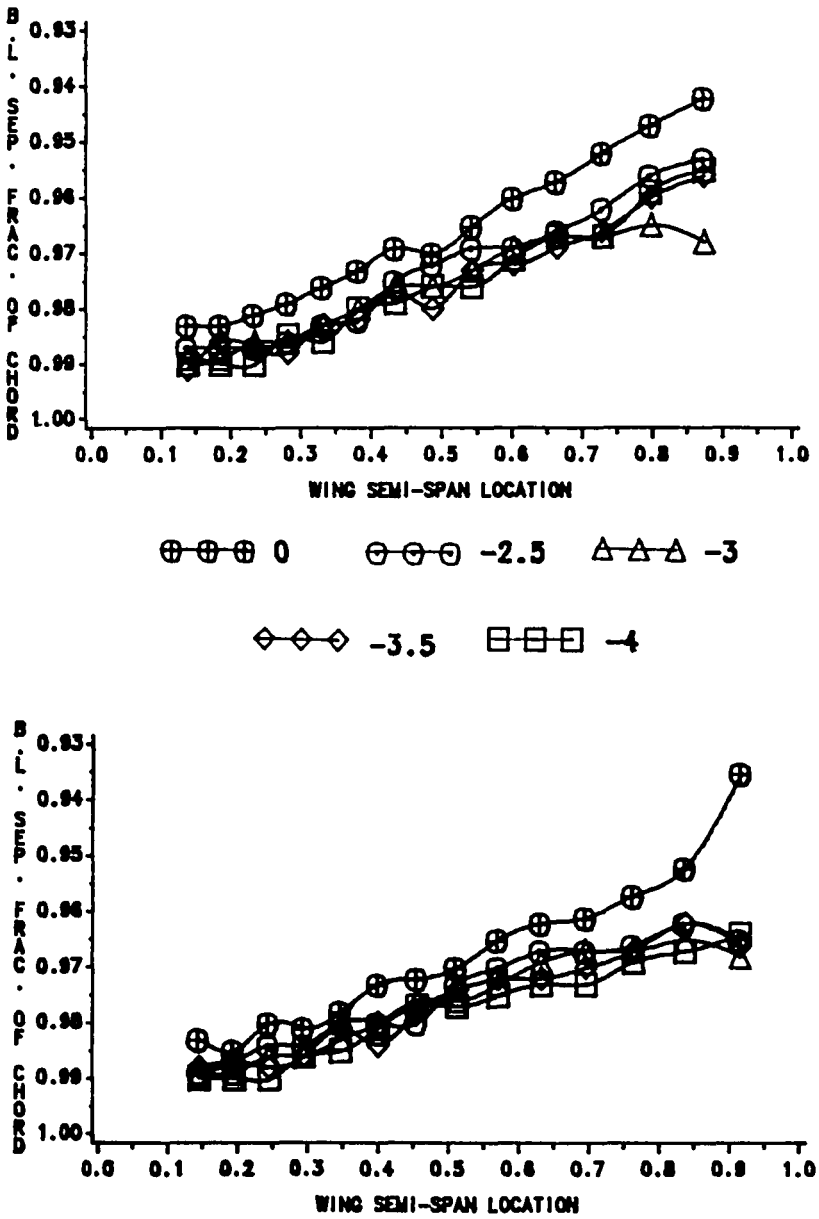

Fig. 24. Predicted upper surface boundary layer separation locations for wing-alone and wing-winglet configurations cropped delta G, wing of wing-winglet and wing-winglet at M = 0.8.

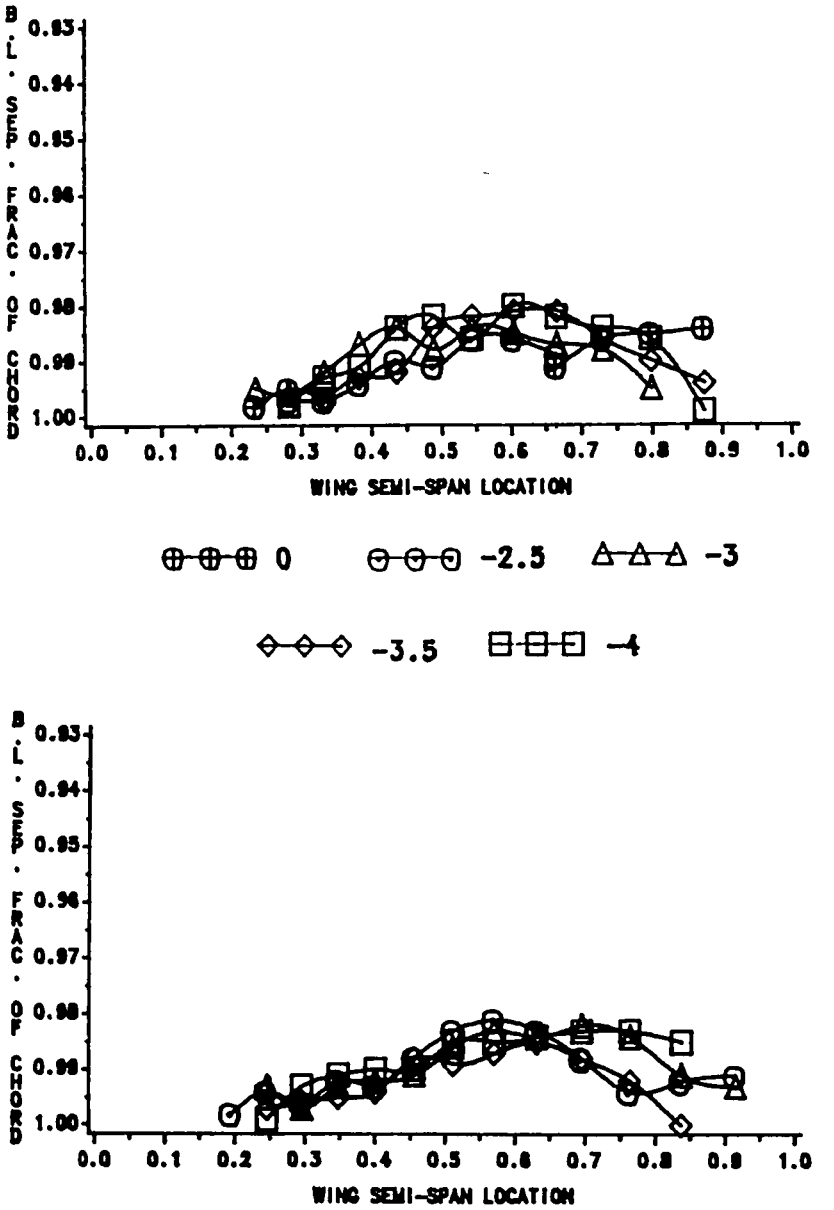

Fig. 25. Predicted upper surface boundary layer separation locations for wing-alone and wing-winglet configurations cropped delta G, optimum wing and modified wing-winglet at M = 0.8.

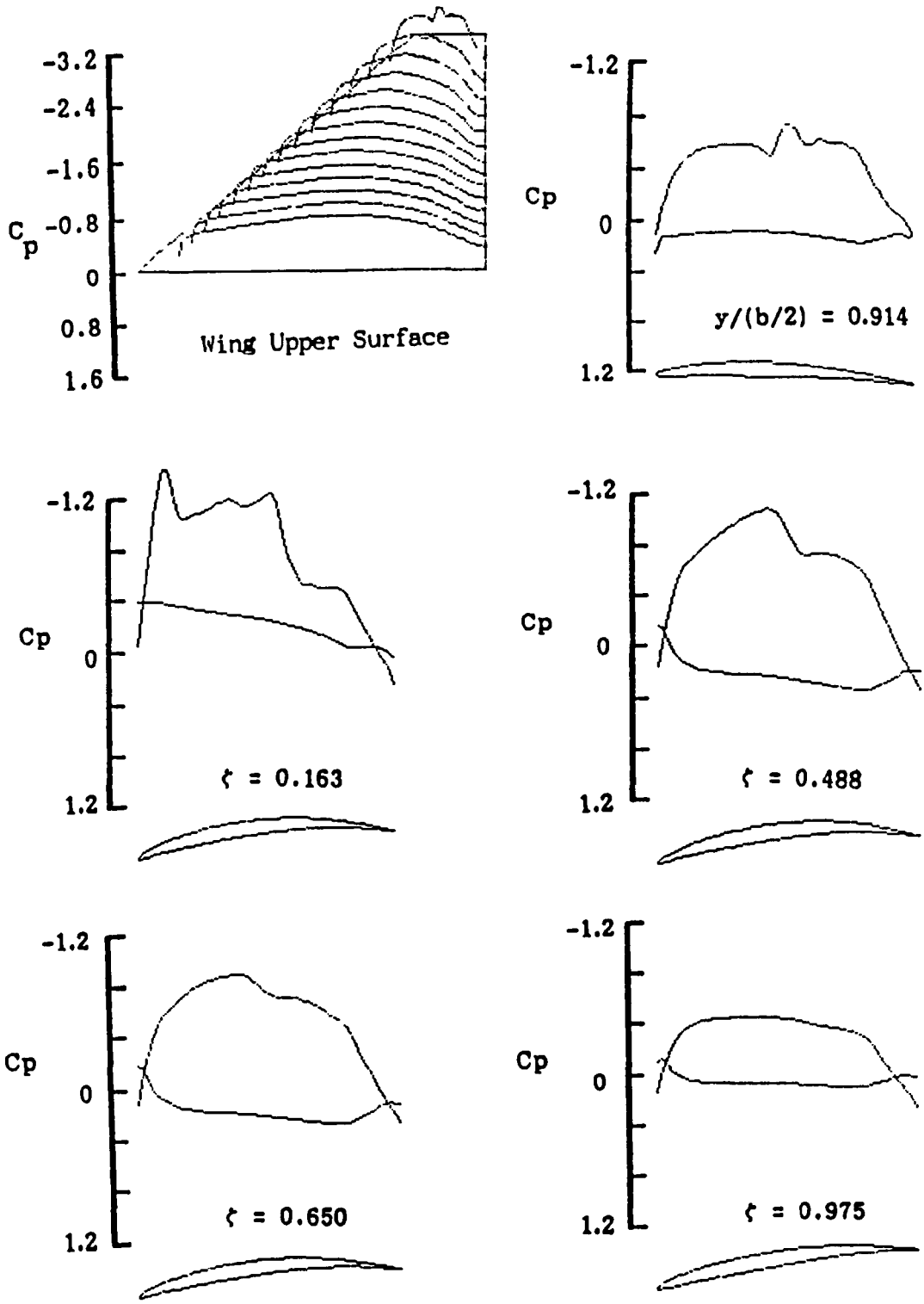

Fig. 26. Calculated wing-winglet C_p distributions for configuration cropped delta G at M = 0.8, α = 0°.

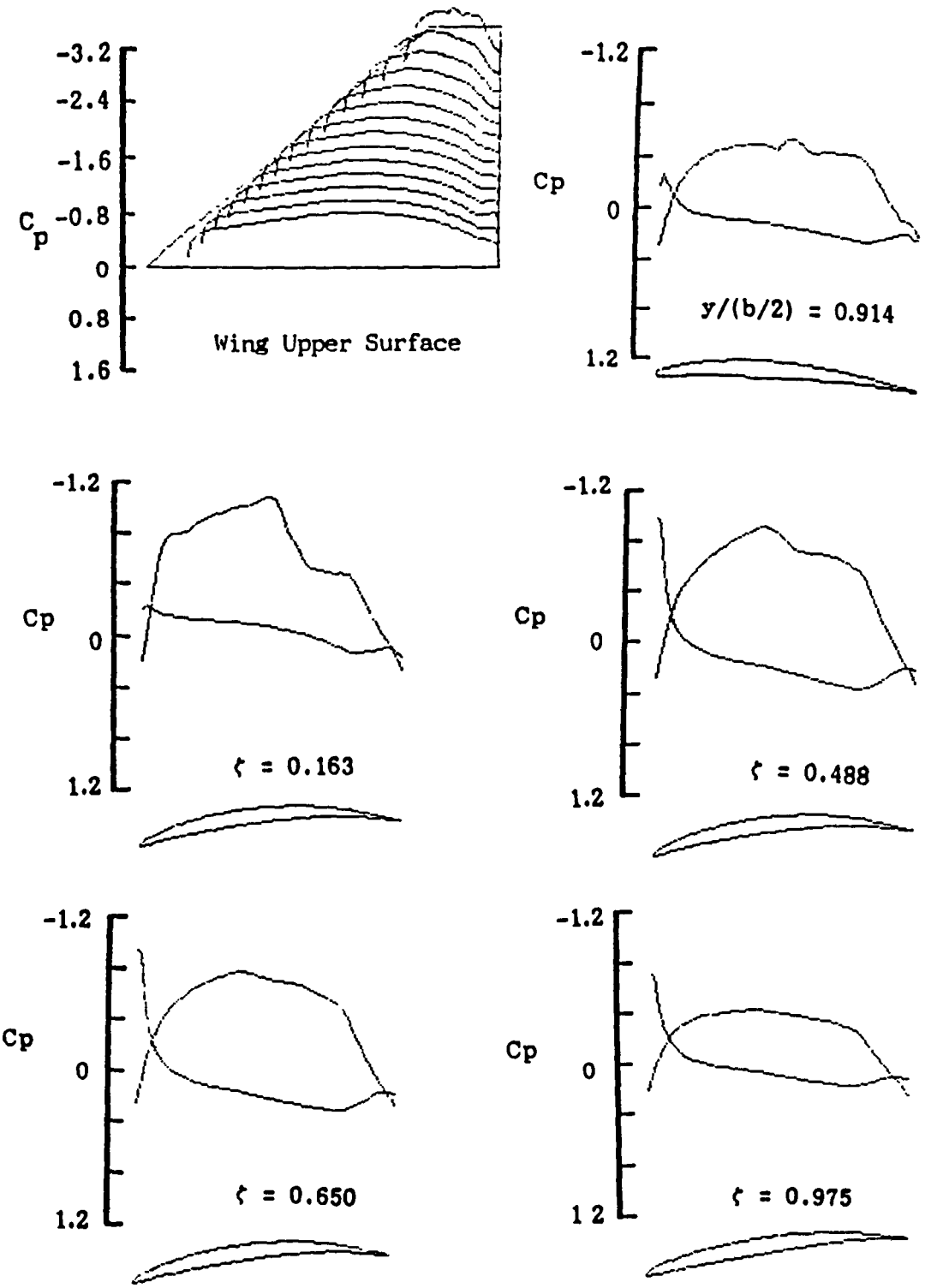

Fig. 27. Calculated wing-winglet C_p distributions for configuration cropped delta G at M = 0.8, α = -2°.

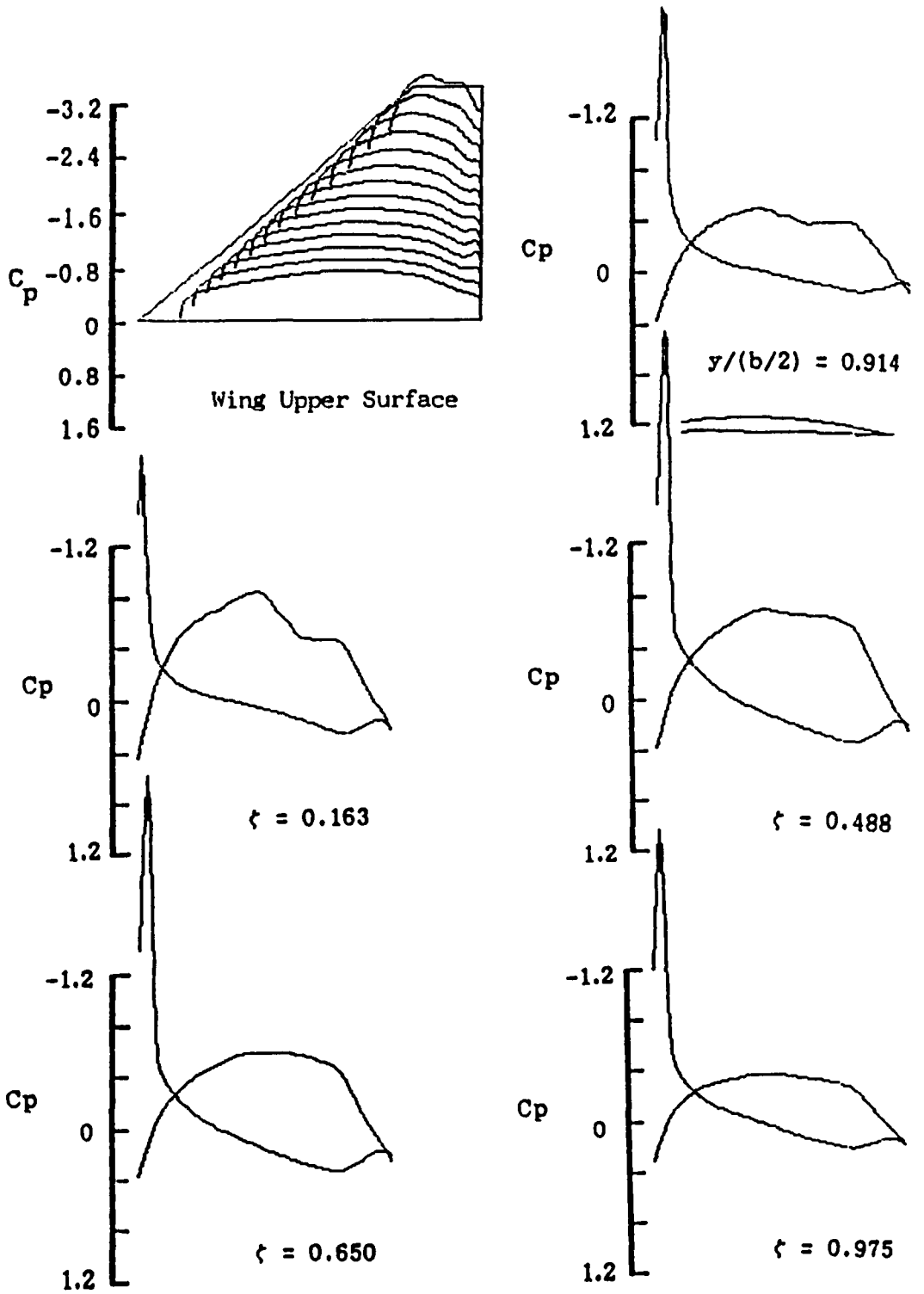

Fig. 28. Calculated wing-winglet C_p distributions for configuration cropped delta G at M = 0.8, α = -4°.

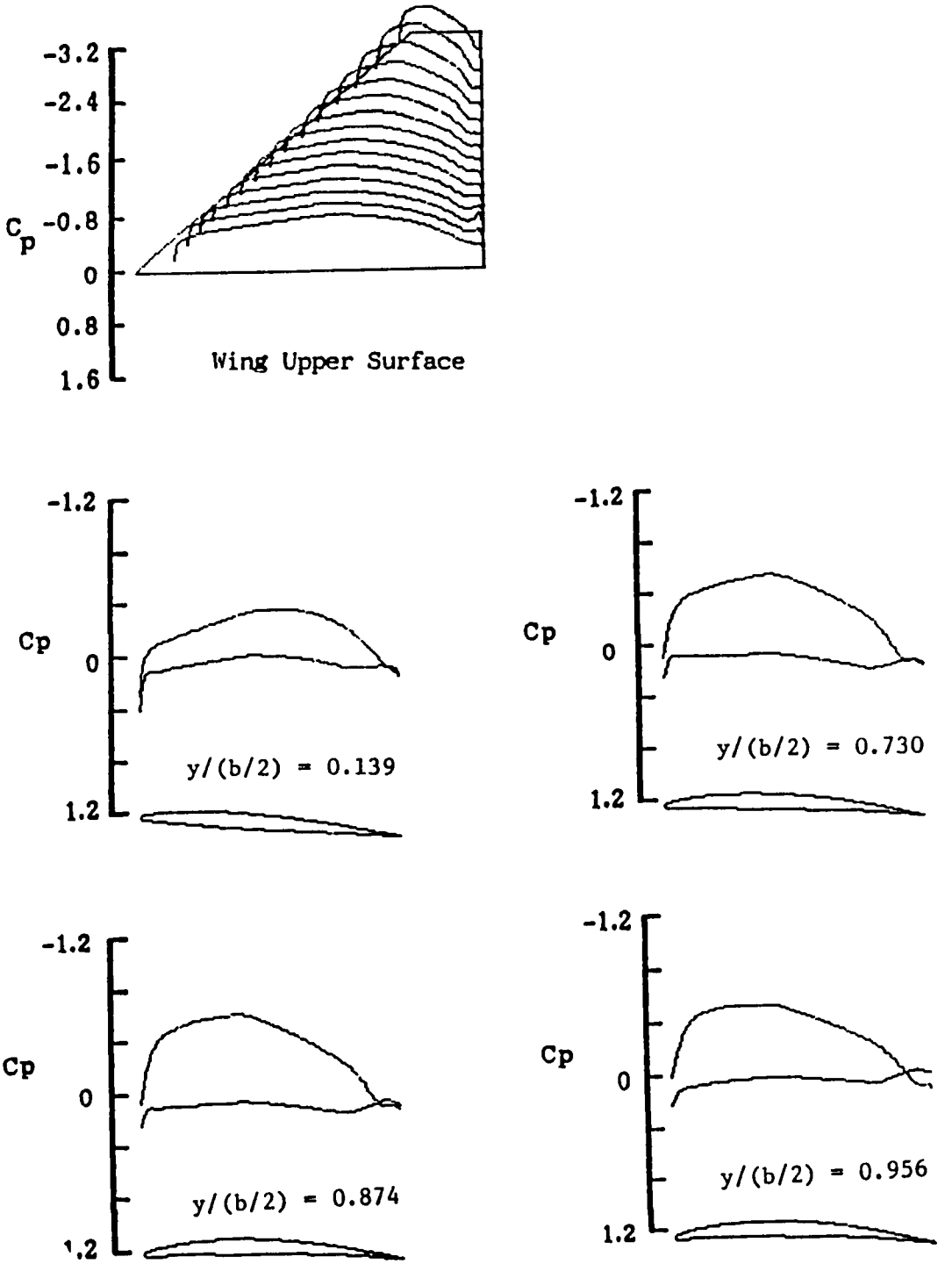

Fig. 29. Calculated wing-alone C_p distributions for wing of cropped delta G wing-winglet at M = 0.8, α = 0°.

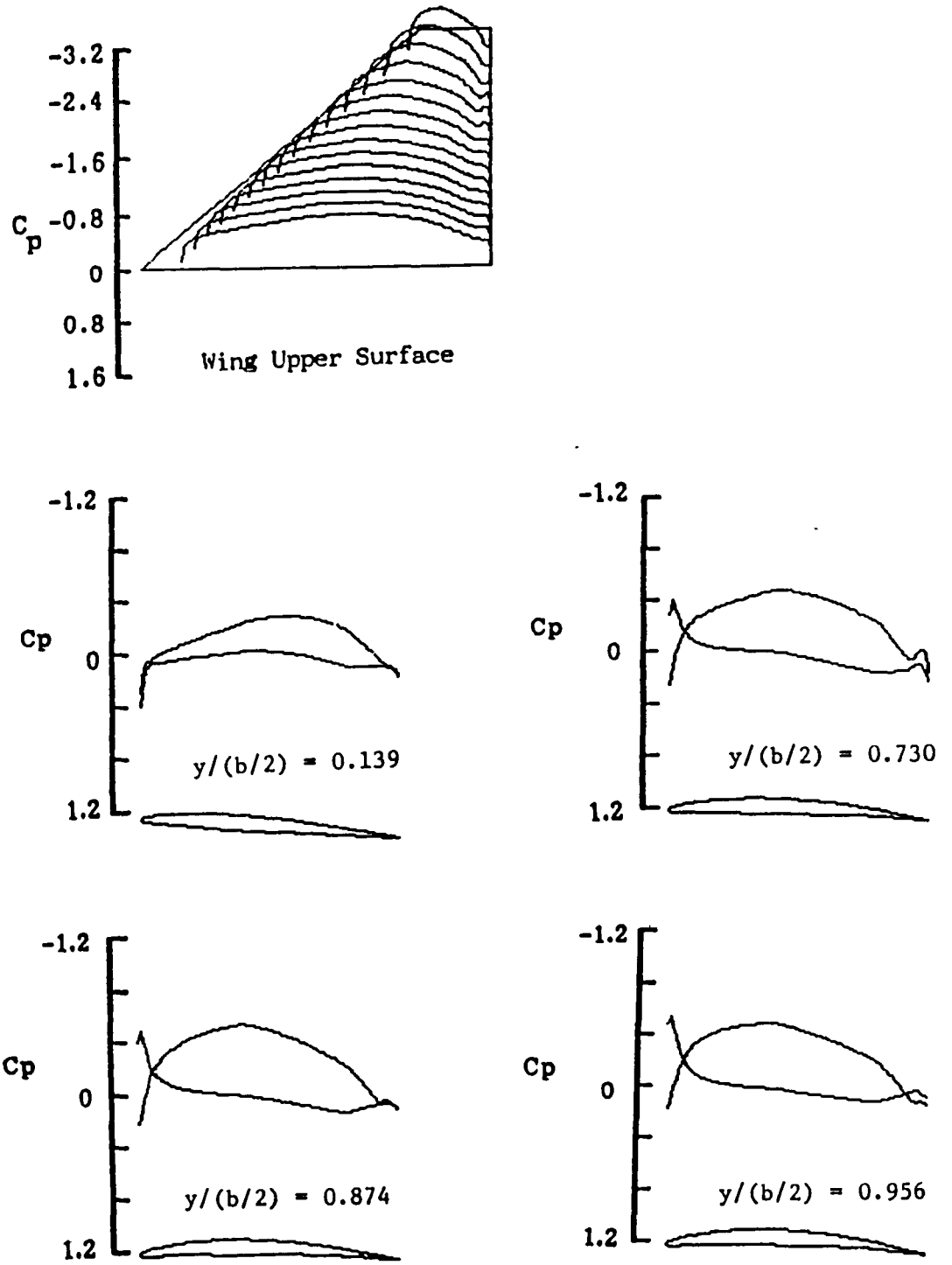

Fig. 30. Calculated wing-alone C_p distributions for wing of cropped delta G wing-winglet at M = 0.8, α = -2°.

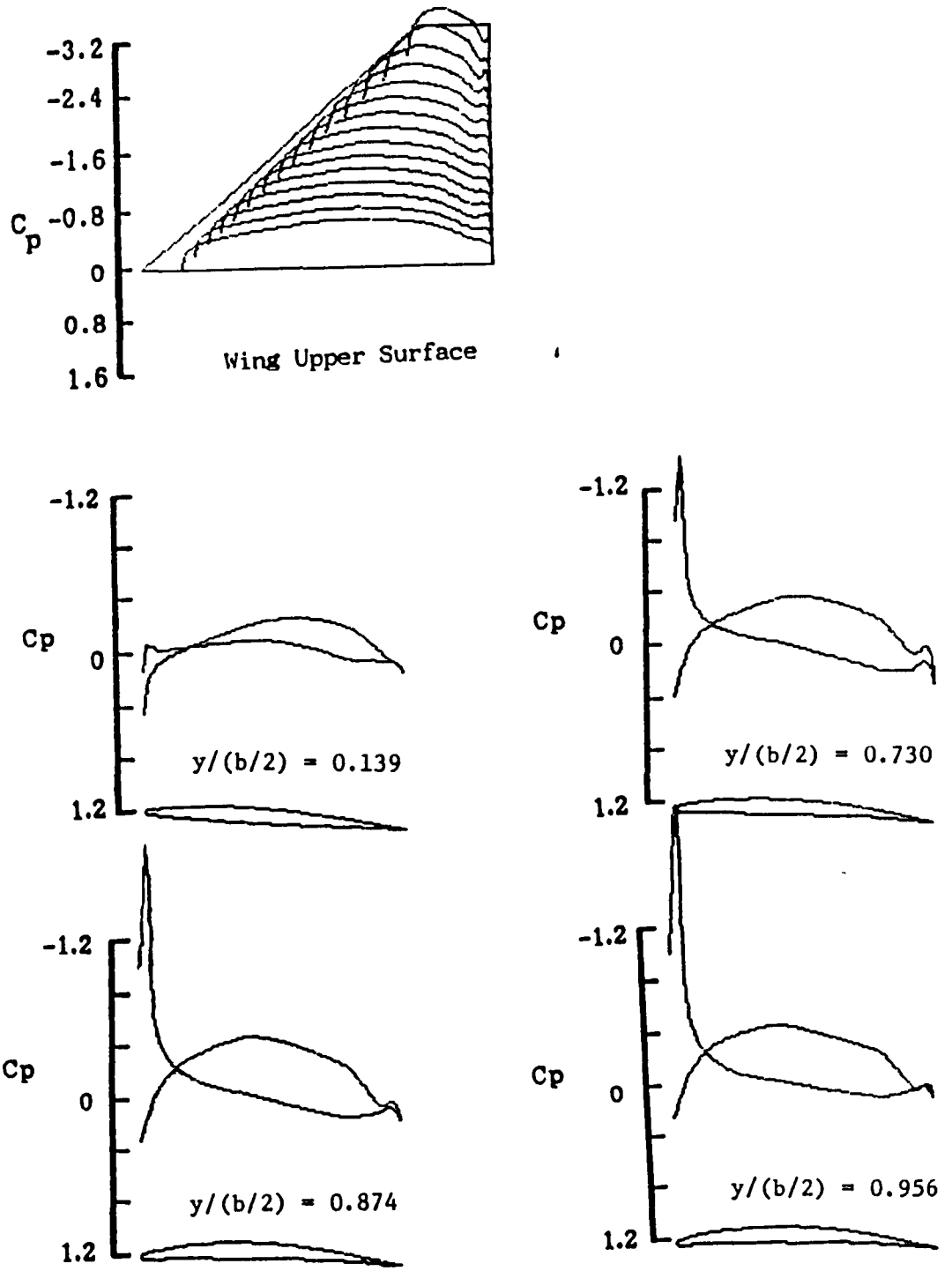

Fig. 31. Calculated wing-alone C_p distributions for wing of cropped delta G wing-winglet at M = 0.8, α = -4°.

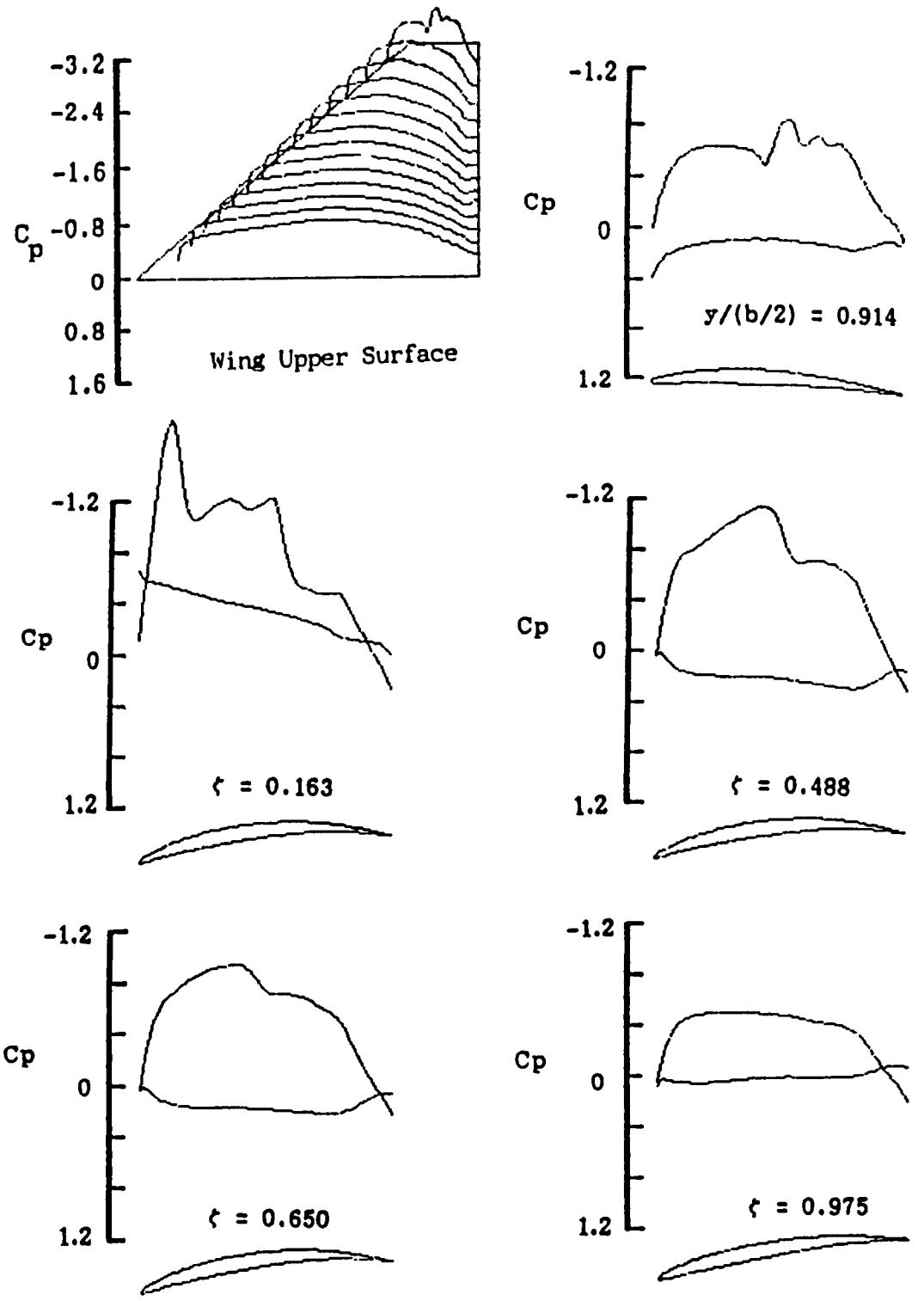

Fig. 32. Calculated wing-winglet C_p distributions for configuration modified cropped delta G at M = 0.8, α = +1°.

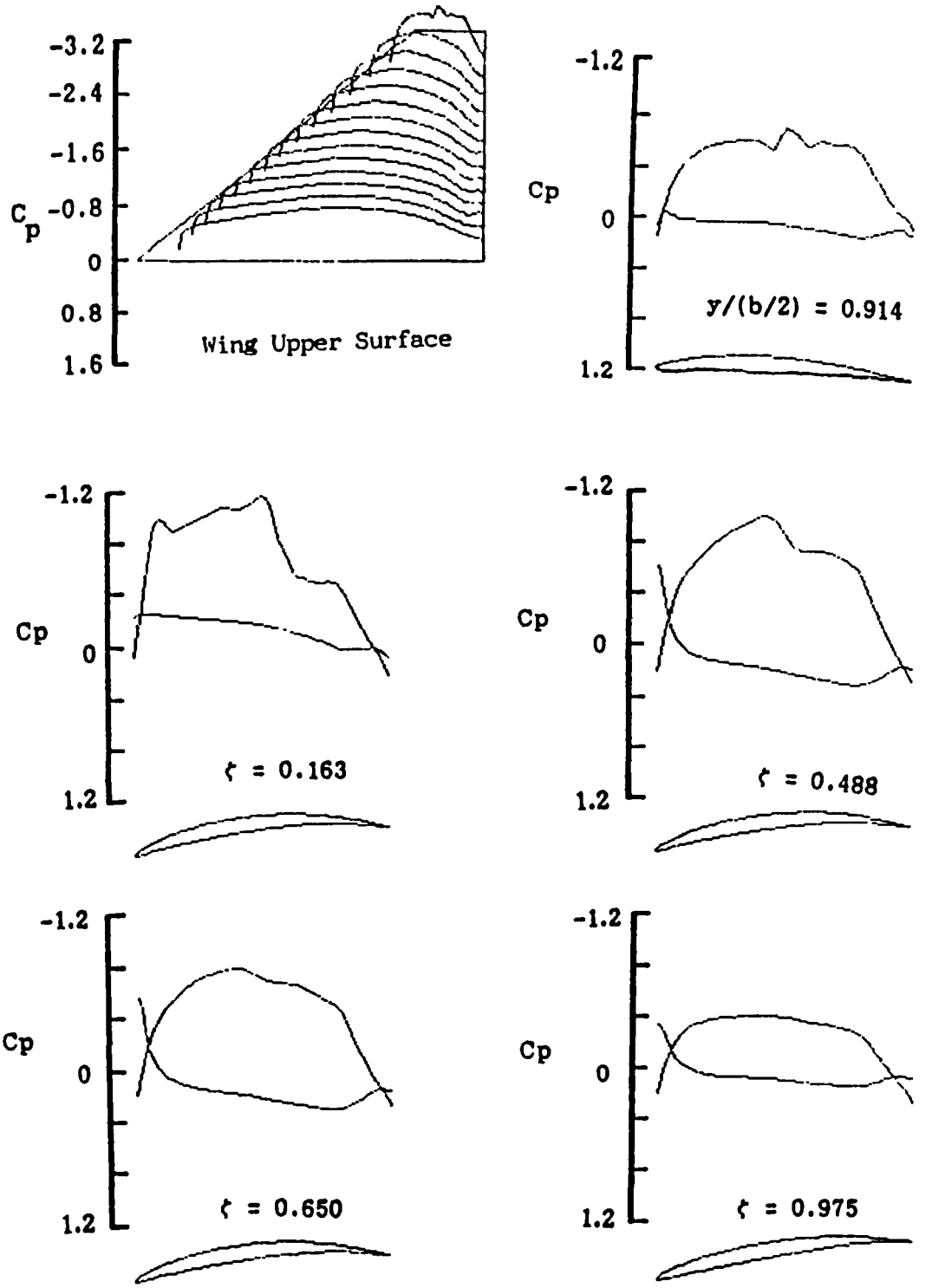

Fig. 33. Calculated wing-winglet C_p distributions for configuration modified cropped delta G at M = 0.8, α = -0.5°.

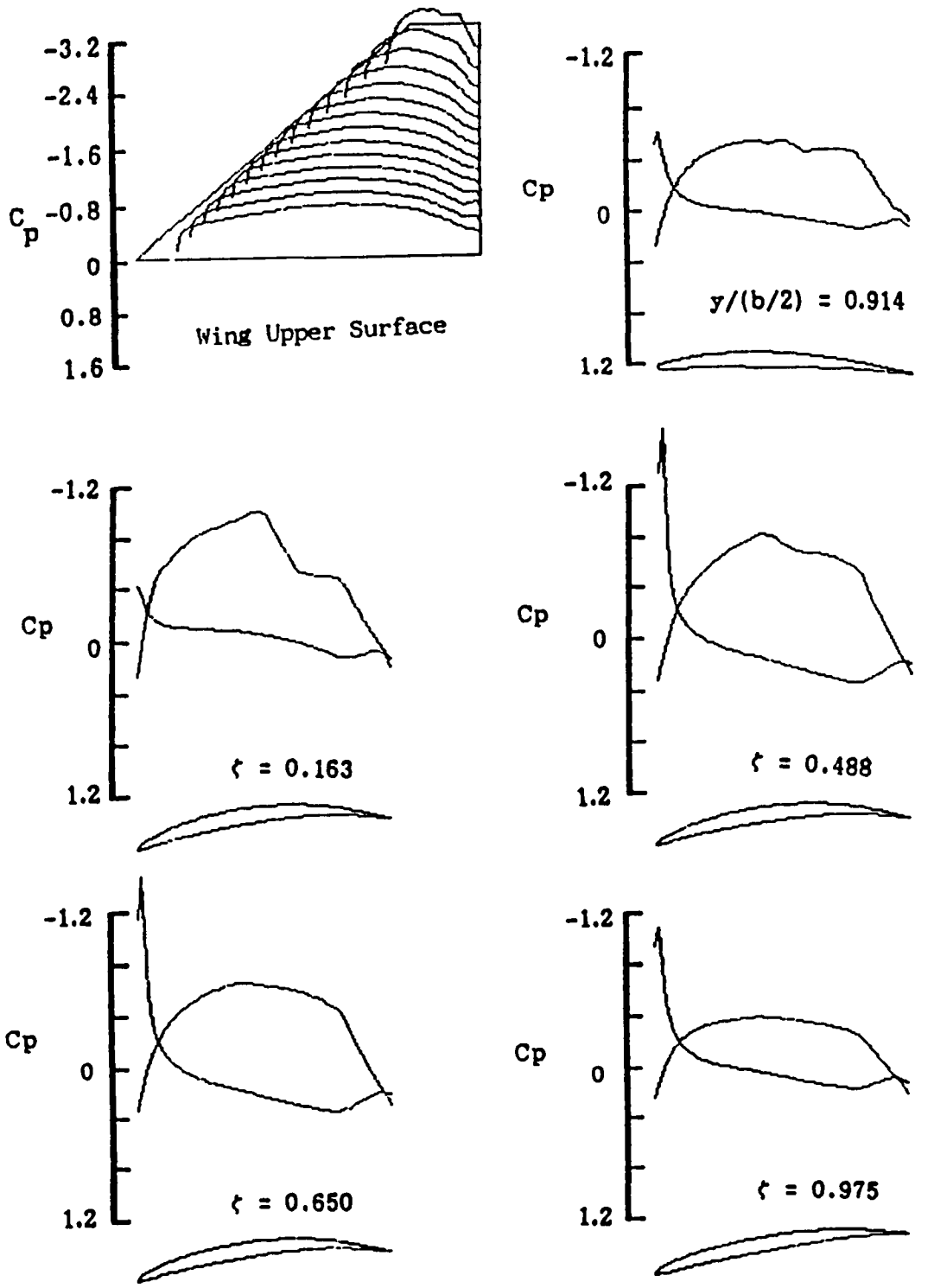

Fig. 34. Calculated wing-winglet C_p distributions for configuration modified cropped delta G at M = 0.8, α = -2°.

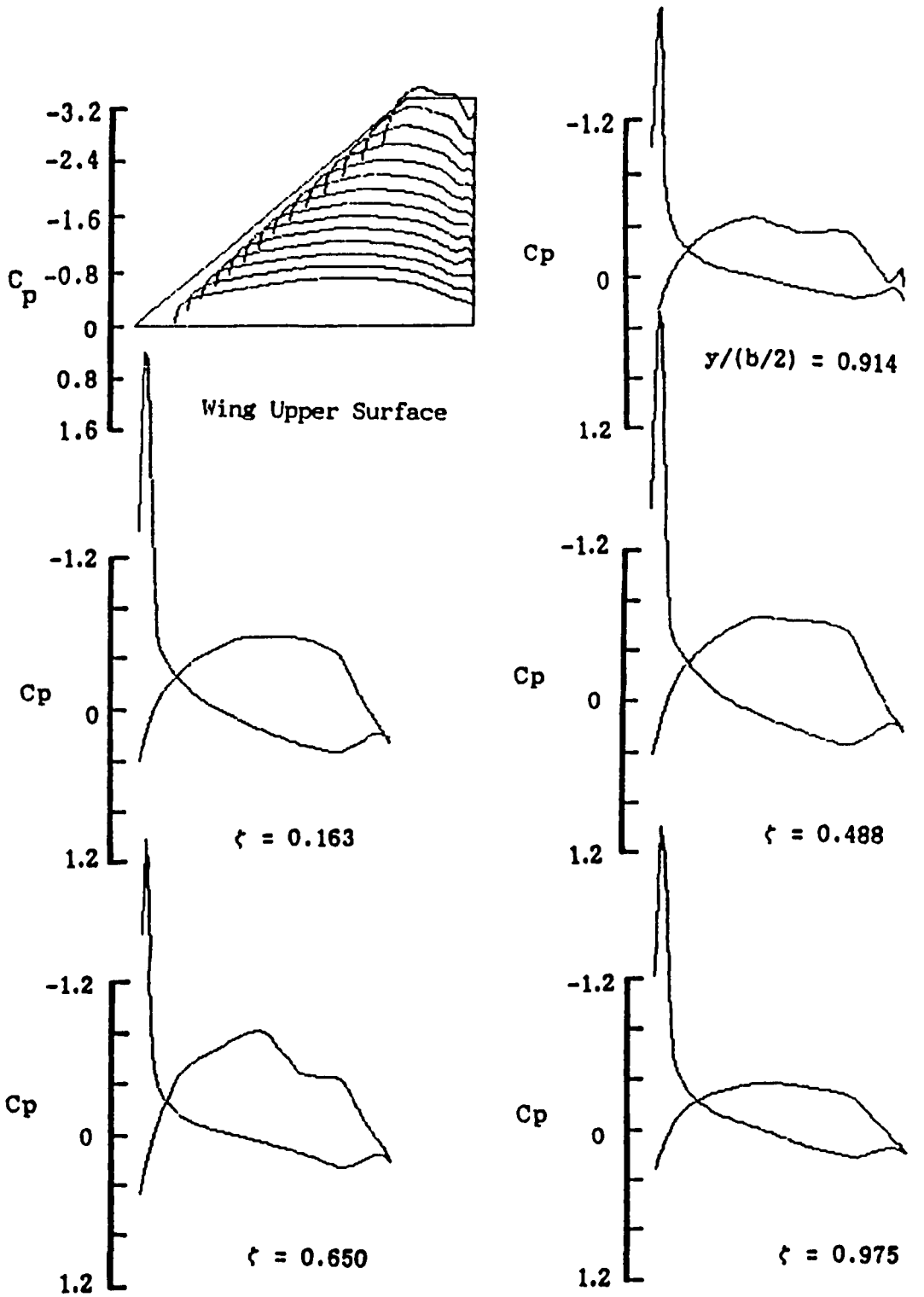

Fig. 35. Calculated wing-winglet C_p distributions for configuration modified cropped delta G at M = 0.8, $\alpha = -4°$.

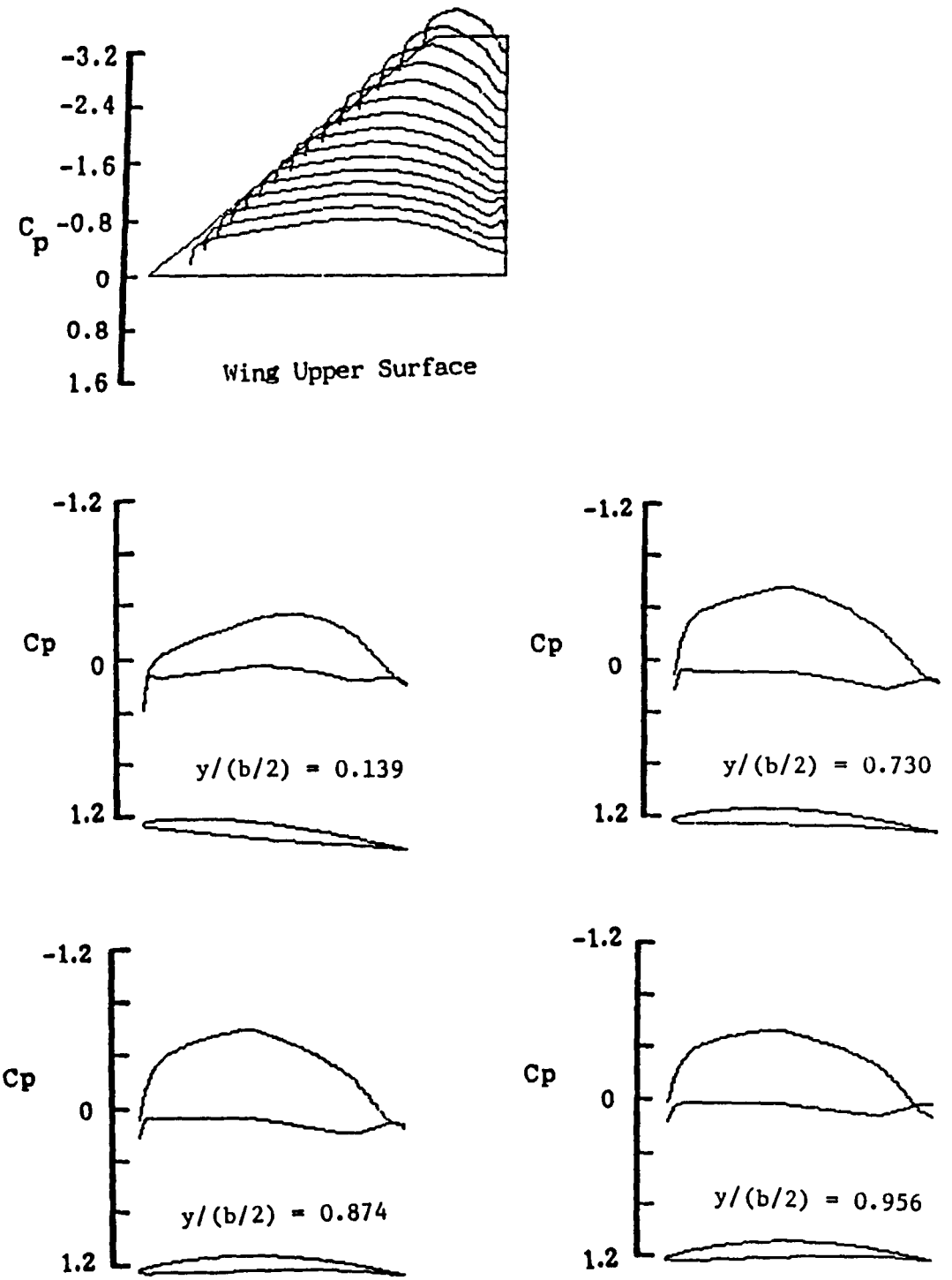

Fig. 36. Calculated wing-alone C_p distributions for configuration cropped delta G at M = 0.8, α = 0°.

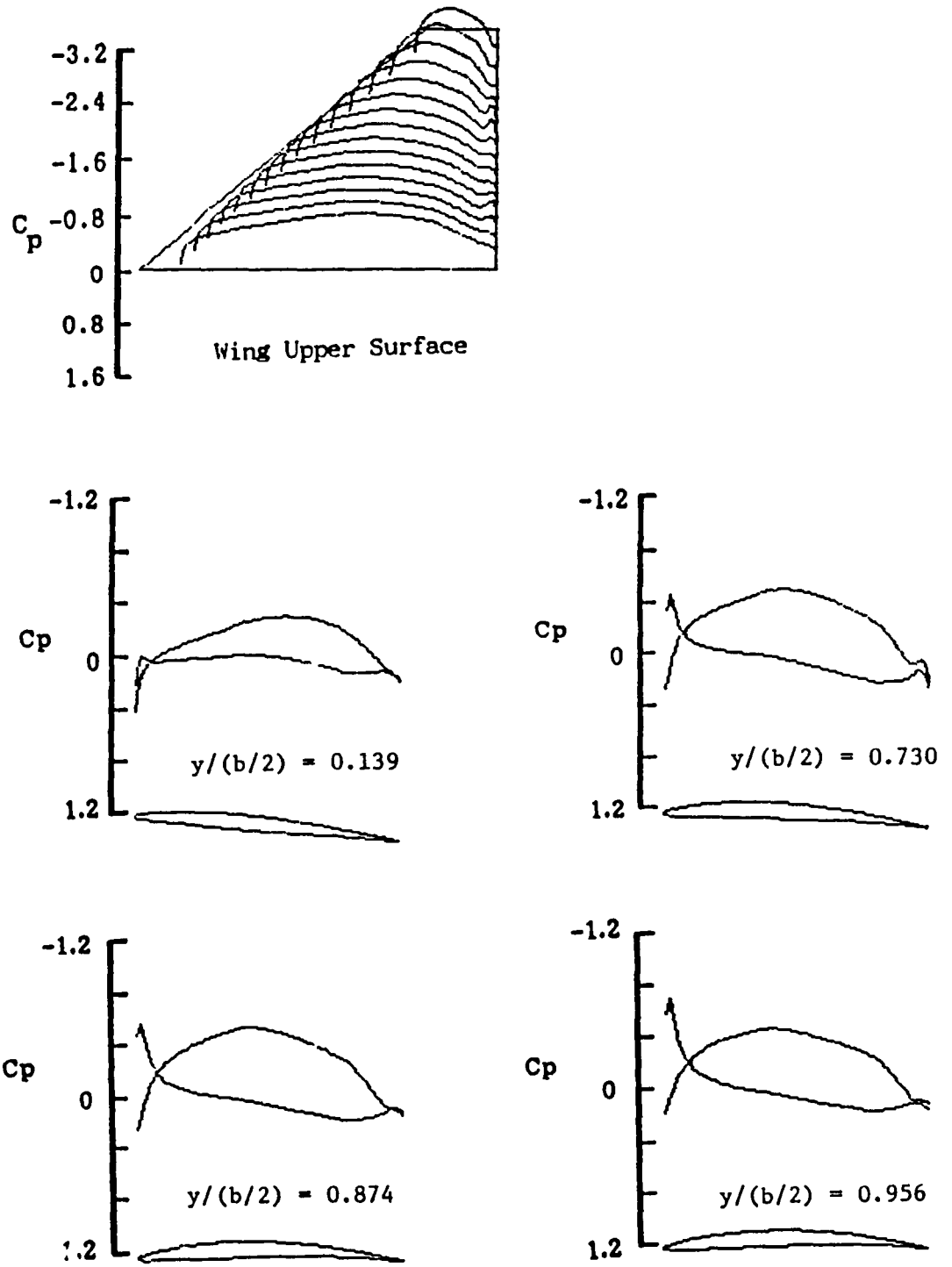

Fig. 37. Calculated wing-alone C_p distributions for configuration cropped delta G at M = 0.8, α = -2°.

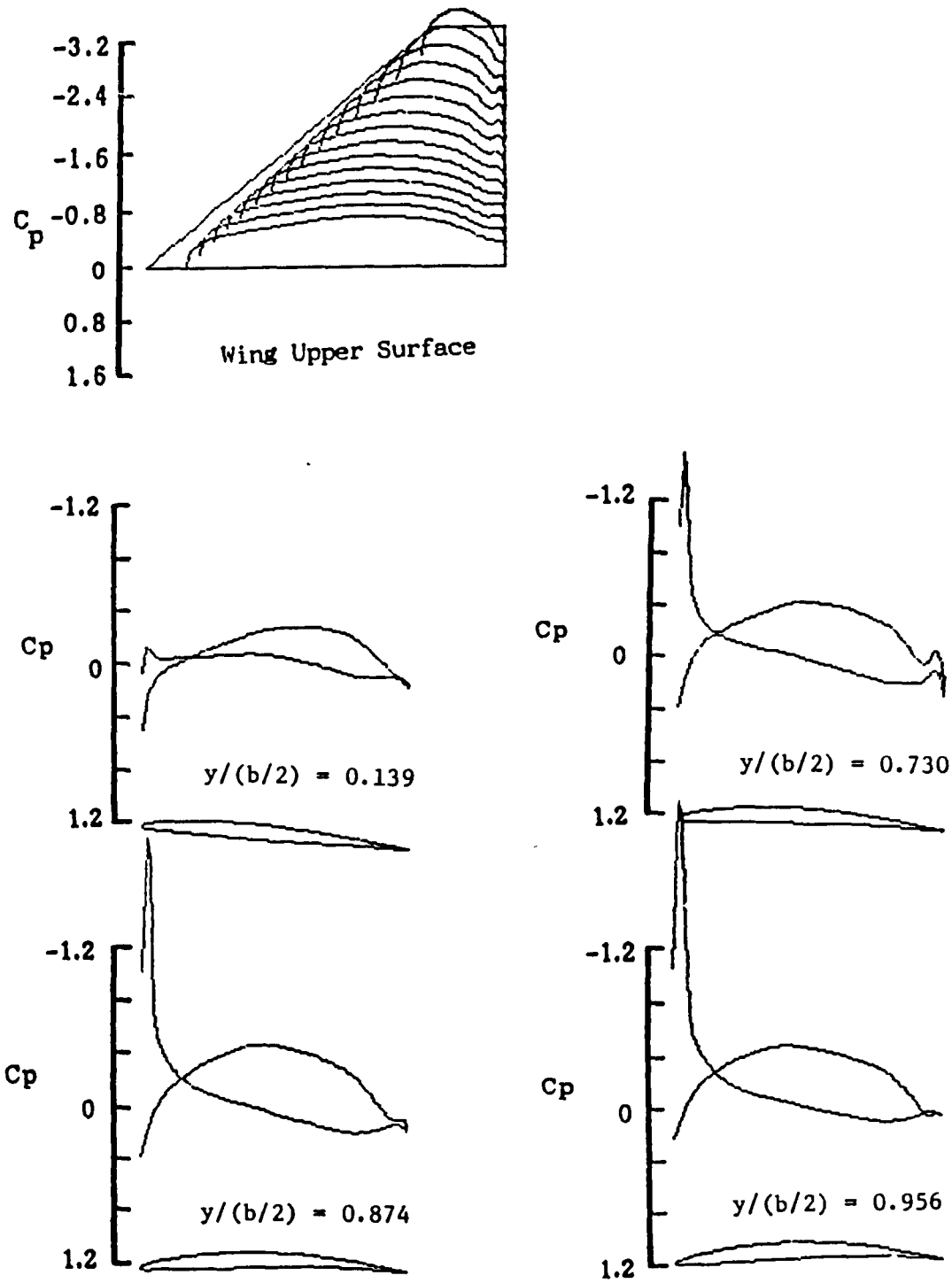

Fig. 38. Calculated wing-alone C_p distributions for configuration cropped delta G at M = 0.8, α = -4°.

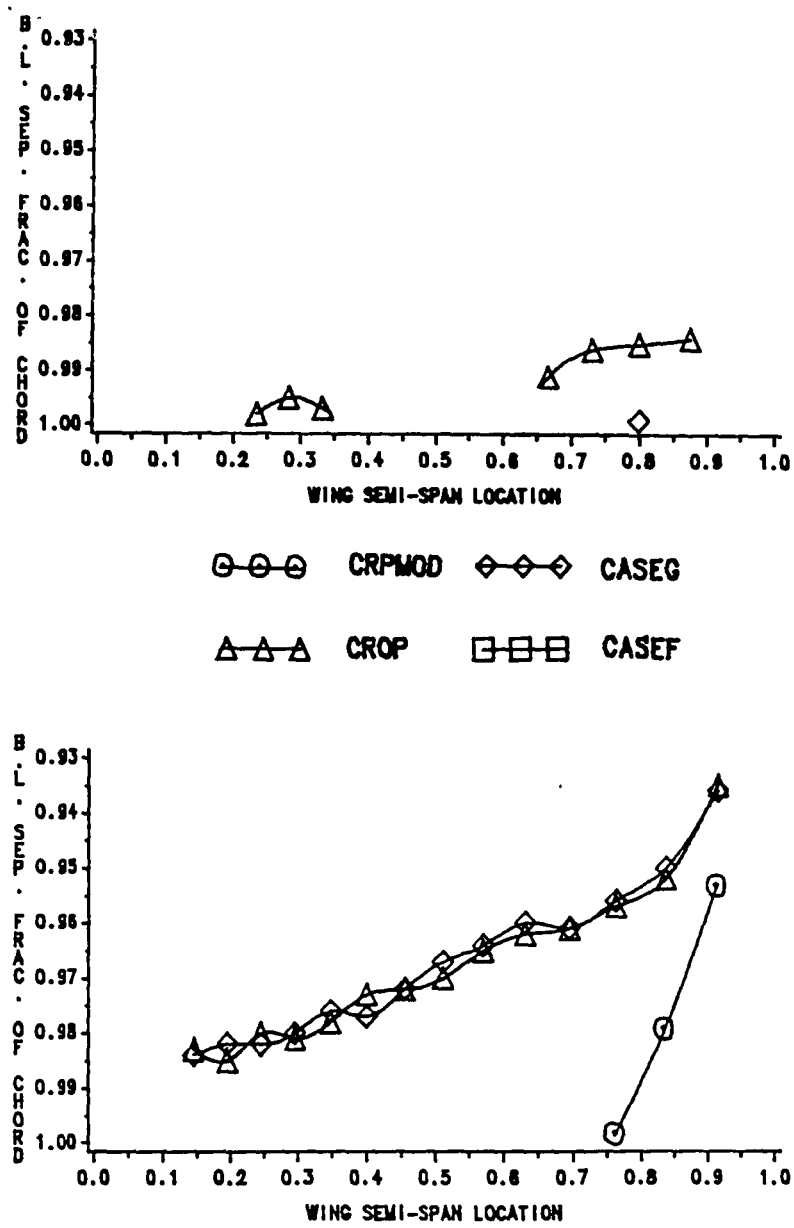

Fig. 39. Predicted upper surface boundary layer separation locations for all wing-alone and wing-winglet configurations at M = 0.8, α = 0° (modified cropped delta G results at α = -0.5°).

End of Document